Mathematical modelling predicts synergistic anti-tumor effects of combining chemotherapy with a macrophage-based, hypoxia-targeted, gene therapy

Supplementary Material

Markus R Owen[1,*], I Johanna Stamper[1,2], Munitta Muthana[3], Giles W Richardson[4], Jon Dobson[5,6], Claire E Lewis[3] and Helen M Byrne[1]

[1] Centre for Mathematical Medicine and Biology, School of Mathematical Sciences, University of Nottingham, Nottingham NG7 2RD, UK.

[2] Department of Physics, University of Alabama at Birmingham, Birmingham, AL 35294-1170, USA.

[3] Department of Infection & Immunity, University of Sheffield Medical School, Beech Hill Road, Sheffield, S10 2RX, UK.

[4] School of Mathematics, University of Southampton, Southampton, SO17 1BJ, UK.

[5] Institute for Science and Technology in Medicine, Keele University School of Medicine, Stoke-on-Trent, ST4 7QB, UK.

[6] Department of Materials Science & Engineering, University of Florida, Gainesville, Florida USA

[*] Corresponding author, email: markus.owen@nottingham.ac.uk

Contents

A Multiscale model for vascular tissue growth and therapy

Our multiscale model for macrophage-based cancer therapy is based upon a model for vascular tumour growth that is described in detail in [45], and incorporates processes that occur on different scales (in space and time). In this model, the vascular configuration, the diffusible chemicals, the cellular layer and the intracellular processes are coupled, as illustrated in Figure S1. For example,

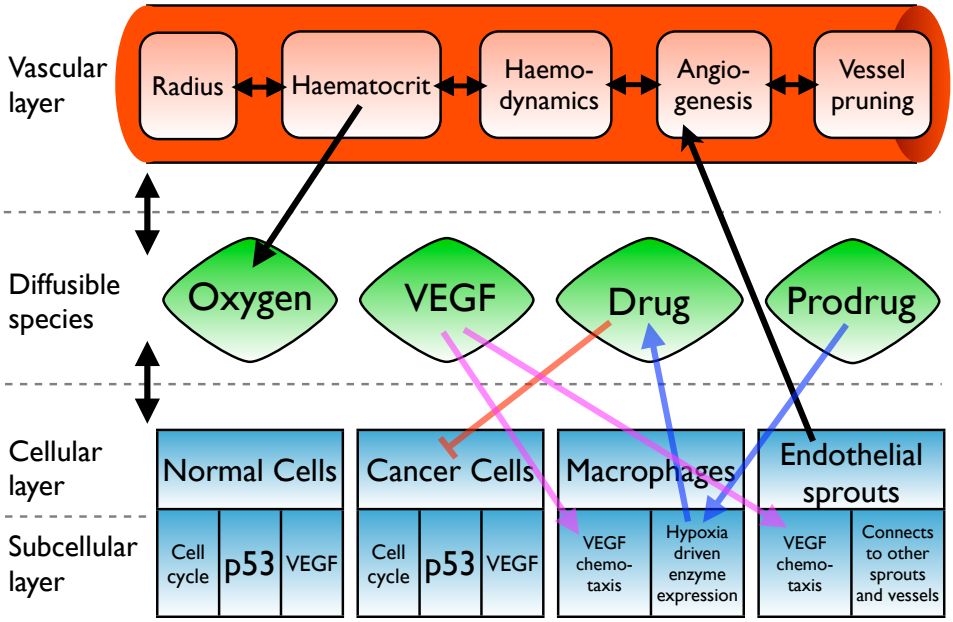

Figure S1: Outline of the mathematical model framework for macrophage-based cancer therapy. Key interactions are shown, in particular that tissue oxygen is regulated by the vascular layer, that Vascular Endothelial Growth Factor (VEGF) drives angiogenesis and macrophage migration, that drug kills tumour cells, and that hypoxic macrophages activate prodrug under hypoxia.

the diffusive transport of oxygen (whose concentration is modelled via a reaction-diffusion equation) provides indirect coupling between the vascular and cellular layers of the tissue, while intracellular processes (here modelled by systems of ordinary differential equations (ODEs)) affect individual cellular processes such as cell division and cell death. In the following, we summarise the original model features from [45], and provide full details of the model extensions to include conventional chemotherapy and macrophage-based gene therapy (including its enhancement using magnetic nanoparticles). A flowchart of the computational algorithm is shown in Figure S2, and for each scale we summarise the components in their temporal order within the algorithm.

A.1 Cellular and subcellular layers

The cellular layer consists of a regular grid of $M \times N$ square lattice sites, of side length Δx. In this paper all simulations are on a 51×51 grid. Each site may contain multiple cells, the number at a given location depending on the cell types and the processes in which they are engaged. For example, each cell type has distinct carrying capacities for movement, N_m, and cell division, D_m [45] (see below for further details on how cell division and movement are simulated).

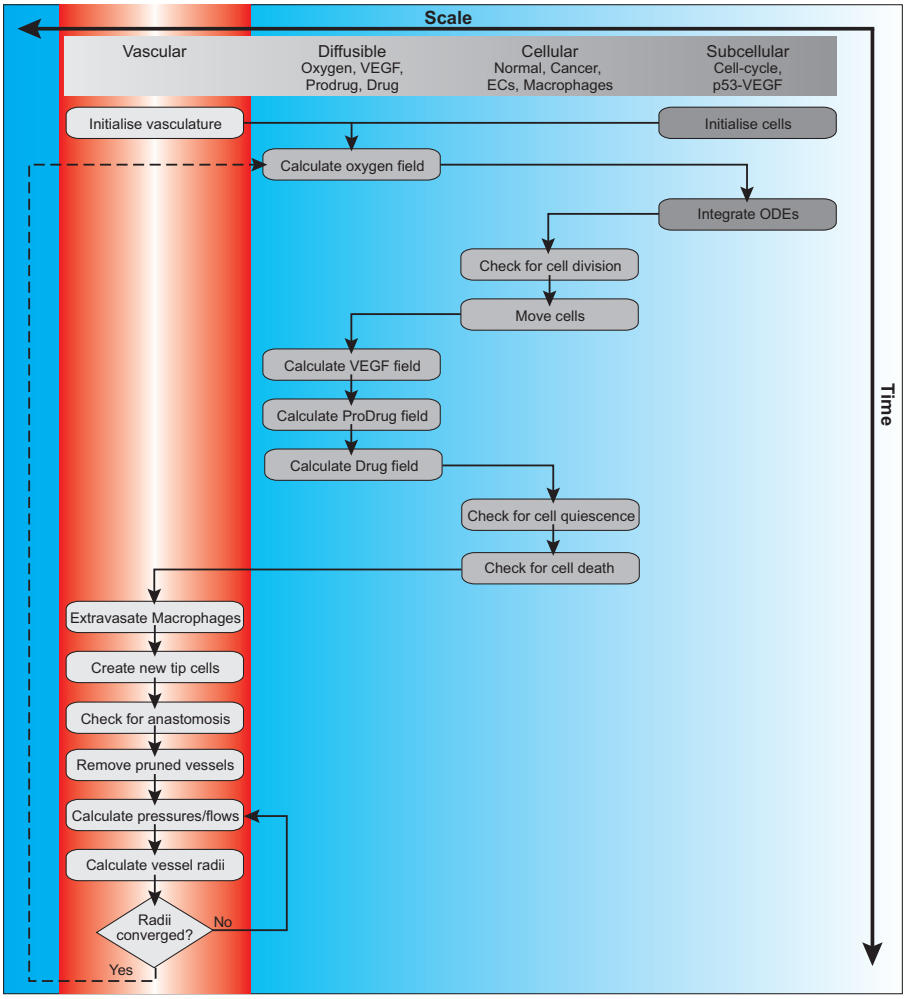

Figure S2: Flowchart of the model algorithm. For each scale we summarise, in this supplementary material, the components in their temporal order within the flowchart.

Some of the processes that occur at the cellular layer depend crucially on the cells' internal states. For example, whether a cell undergoes apoptosis depends on its intracellular level of p53. The dynamics of p53, intracellular VEGF (which influences VEGF secretion) and progress through the cell cycle are modelled in the subcellular layer by systems of time-dependent ODEs, which are integrated on each time step of the model simulation.

A.1.1 Initialisation

The lattice is initially populated with a user-specified set of cells. For the simulations in this paper, normal tissue is generated by adding one normal cell to each lattice site. A tumour is implanted by replacing normal cells with cancer cells in a rectangle of lattice sites ($[11, 16] \times [36, 41]$). All cells are given an initial cell cycle phase of zero (see next section).

A.1.2 Integrate cell cycle and p53-VEGF ODEs for normal and cancer cells

The cell cycle model used in [45] was a system of 5 ODEs, originally developed by Alarcón and co-workers [2] as an extension of the eukaryotic cell cycle model by Tyson and Novak [65]. In [2], the oxygen concentration affects the cell cycle via its regulation of p27—hypoxia upregulates p27 which inhibits cyclin-CDK formation and thus cell cycle progression [2]. Hence the cell cycle time

is a decreasing function of oxygen concentration at the cell's current tissue location, $C(\mathbf{x}, t)$. In addition, cancer cells are assumed to enter and leave quiescence at certain threshold values of their p27 concentration.

In order to increase the speed of simulations, we replace the system of 5 ODEs with a simple phase model in which $\phi(t) \in [0, 1]$ represents the phase of the cell cycle, with

$$\frac{d\phi}{dt} = \frac{C}{T_{\min}(C_\phi + C)}, \tag{A1}$$

and the reset condition that when $\phi = 1$ it is reset to zero (so that $\phi = 0$ represents the start of the cell cycle, and $\phi = 1$ its completion). In equation (A1) the right hand side specifies the speed of progress through the cycle as a function of oxygen concentration, C. Here, and in the subcellular model for p53-VEGF regulation, we suppress the notation for the spatiotemporal dependence of oxygen, $C = C(\mathbf{x}, t)$, and it is implicit that by C we mean the oxygen concentration in a cell at a particular lattice site. $T_{\min}$ is the minimum period of the cell cycle (in nutrient rich conditions), and C_ϕ is the oxygen concentration at which the speed is half maximal. As $C \to \infty$, $d\phi/dt \to 1/T_{\min}$ so that ϕ increases from zero to one in time $T_{\min}$. We derive the parameters for this reduced model from the oxygen dependent cell cycle time data illustrated in [3]—i.e. we ensure that our simplified model reflects the oxygen dependence seen in the full model.

We remark that in [2, 45] the oxygen concentration in the subcellular models is dimensionless. Here we introduce the scaling $C_{dim} = (C/0.045) \cdot 20\text{mmHg}$, which gives dimensional values of the subcellular parameters (such as C_ϕ) in physiologically realistic ranges. In the tables of parameters we give the relevant parameter values in dimensional form (in mmHg). Figure S3 shows how the cell cycle period given by equation (A1) closely matches that for the full model of Alarcón *et al.* [2].

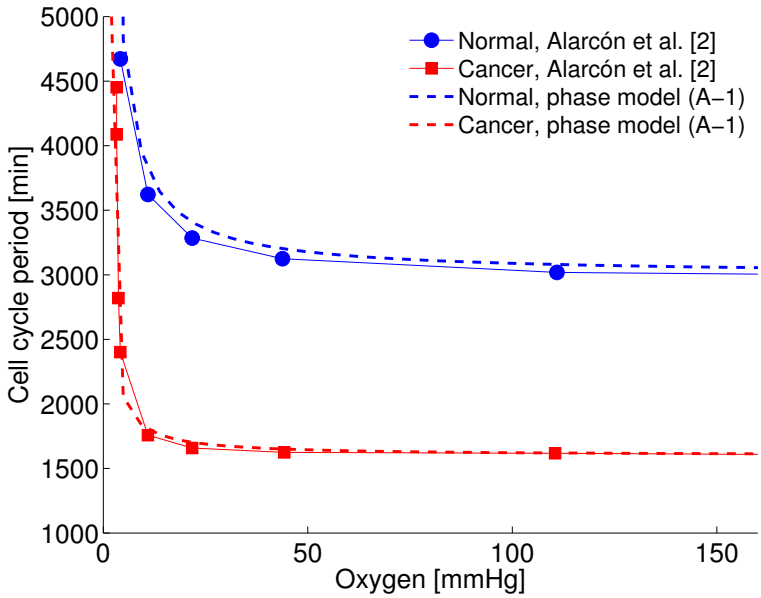

Figure S3: Cell cycle period against oxygen concentration, comparing the results for the full model of Alarcón *et al.* [2] with those for the simplified phase model given by equation (A1). The parameters in equation (A1) are $(C_\phi, T_{\min}) = (3\text{mmHg}, 3000\text{min})$ for normal cells (red crosses), and $(C_\phi, T_{\min}) = (1.4\text{mmHg}, 1600\text{min})$ for cancer cells (blue crosses), as given in Table S2. Here, we assume that $C = 0.045$ corresponds to a typical dimensional perivascular oxygen oxygen tension of 20 mmHg [37], and we apply the same scaling to the results from Alarcón *et al.* [2].

On each time step the cell cycle state variable is updated by integrating the ODE (A1) for time Δt, assuming that the oxygen concentration (and hence the rate of progression through the cycle) is constant during that time period.

The intracellular levels of the tumour suppressor gene p53, $[p53]$, and VEGF, $[VEGF]$, are modelled in all normal cells by a pair of ODEs, with hypoxia upregulating both p53 and VEGF [3, 45], and high levels of p53 inhibiting VEGF production. On each time step the intracellular p53 and VEGF variables are updated by integrating the ODEs for time Δt.

The evolution of the concentrations of p53 and VEGF within a given cell are modulated by oxygen in the following manner:

$$\frac{d[p53]}{dt} = k_7 - k_7^{'}\frac{C}{C_{p53}+C}[p53] \tag{A2}$$

$$\frac{d[VEGF]}{dt} = k_8 + k_8^{''}\frac{[p53][VEGF]}{J_5+[VEGF]} - k_8^{'}\frac{C}{C_{VEGF}+C}[VEGF]. \tag{A3}$$

Here, $k_8^{''}$ is negative for normal cells (p53 decreases VEGF production in normal cells). Oxygen promotes p53 and VEGF degradation, and their expression therefore increases under hypoxia. In [3, 45], cancer cells have a mutation such that $k_8^{''}$ is positive (p53 increases VEGF production). However, cancer cells are also assumed to be resistant to apoptosis via elevated p53 [3, 45], and this submodel is effectively redundant for cancer cells. For details of the experimental evidence supporting these forms we refer the reader to [3].

Apoptosis is triggered in normal cells if $[p53]$ is too high (see Section A.1.6 below). When $[VEGF] > V_{THR}$, VEGF is released by normal cells into the extracellular space, acting as a local source of extracellular VEGF, $V(\mathbf{x}, t)$ (see Section A.2.2).

A.1.3 Cell division

If the phase, ϕ, of a cell at $\mathbf{x}$ reaches one (the internal condition for division to occur), a check is carried out to ensure that enough space is available at $\mathbf{x}$ for a daughter cell. If in the current location the number of cells is less than the carrying capacity for cell division (i.e. if $N(\mathbf{x}, t) < D_m$), the daughter cell is placed there. If no space is available ($N(\mathbf{x}, t) \geq D_m$), then neighbouring sites are checked for space. If there is space at a site in the Moore neighbourhood of $\mathbf{x}$, then the daughter cell is placed in the neighbouring site where the oxygen concentation is the highest. Upon successful division, the parent and daughter cells have their cell cycle phases set to zero. If there is insufficient space to complete cell division, the parent cell cycle phase is reset to zero, and no daughter cell is produced.

If the phase, ϕ, reaches one, and there is space to divide, but the cell has previously intercalated drug, then cell division is aborted (intercalated drug interferes with DNA replication) and the mother cell dies. See section A.6 below.

A.1.4 Cell movement

Cell movement, via a reinforced random walk, is implemented by looping through all active cells and assigning probabilities for moving from a site $\mathbf{x}$ to sites in the Moore neighbourhood of $\mathbf{x}$ (i.e. the eight connected neighbours, including diagonal moves). The probability of a cell moving from lattice

site $\mathbf{x}$ to $\mathbf{y}$ in time Δt, $Pr(\mathbf{x}, \mathbf{y}, t)$, is given by:

$$Pr(\mathbf{x}, \mathbf{y}, t) = \frac{D\Delta t}{2d^2_{\mathbf{x},\mathbf{y}}} \frac{(N_m - N(\mathbf{y}, t))}{N_m} \left(1 + \frac{\chi}{2D} (V(\mathbf{y}, t) - V(\mathbf{x}, t))\right) \quad \text{for} \quad \mathbf{x} \neq \mathbf{y}, \tag{A4}$$

where $N(\mathbf{x}, t)$ is the number of cells at site $\mathbf{x}$, $V(\mathbf{x}, t)$ is the VEGF level at site $\mathbf{x}$. D is the maximum cell motility in the absence of chemotaxis, N_m is the carrying capacity for movement of the cell type attempting to move, χ is the chemotactic sensitivity, and $d_{\mathbf{x},\mathbf{y}}$ is the distance between sites $\mathbf{x}$ and $\mathbf{y}$ (and hence is either Δx or $\sqrt{2}\Delta x$). Equation (A4) is used for all cell types, and random motion without chemotaxis is obtained by setting $\chi = 0$ (e.g. for normal and cancer cells).

This form is simpler than that in [45], and is similar to the volume filling model of Painter and Hillen [47]. The term $(N_m - N(\mathbf{y}, t)$ measures the space available at $\mathbf{y}$. If $N(\mathbf{y}, t) \geq N_m$ then there is no space at the target site, and the movement probability is zero.

For this probability of movement on a Moore neighbourhood, the continuum limit is a diffusion-chemotaxis equation for the cell density $u(\mathbf{x}, t)$:

$$\frac{\partial u}{\partial t} = D\nabla^2 u - \chi \nabla \cdot \left[u \left(1 - \frac{u}{N_m}\right) \nabla V \right]$$

so that, in equation (A4), D and χ correspond to random motility and maximum chemotaxis coefficients respectively, for both of which estimates are available in the literature.

A.1.5 Cell quiescence

In [45] cancer cells enter and leave quiescence according to their intracellular level of p27. As we have introduced the simplified phase model (equation (A1)) for the cell cycle, we replace this p27 dependence with an equivalent dependence on the local oxygen concentration, C.

Cancer cells become quiescent when their local oxygen levels fall too low ($C < C^{\text{enter}}_{\text{quiesc}'}$), and stop being quiescent when the oxygen concentration becomes sufficiently high ($C > C^{\text{leave}}_{\text{quiesc}'}$). When a cell becomes quiescent, a timer $T_{quiescent}$ is set to zero and then incremented by Δt for each time step that the cell remains quiescent. Quiescent cancer cells do not progress through the cell cycle (ϕ is constant during quiescence).

A.1.6 Cell death

Normal cell apoptosis is triggered if intracellular p53 is sufficiently high, $[p53] > p53_{THR}$. The threshold $p53_{THR}$ takes a smaller value ($p53^{low}_{THR}$) when a normal cell is surrounded by more cancer cells (reflecting the assumption that the tumour microenvironment is hostile to normal cells), and otherwise takes a higher value ($p53^{high}_{THR}$).

Thus the threshold depends on the local ratio of normal cells to normal and cancer cells, ρ_{normal}:

$$p53_{THR} = \begin{cases} p53^{high}_{THR} & \text{for} \quad \rho_{normal} > \rho_{THR}, \\ p53^{low}_{THR} & \text{for} \quad \rho_{normal} \leq \rho_{THR}. \end{cases} \tag{A5}$$

Here, ρ_{normal} for a normal cell at location $\mathbf{x}$ is given by

$$\rho_{normal}(\mathbf{x}) = \frac{\sum_{\mathbf{y} \in \Theta_{\mathbf{x}}} \text{number of normal cells at site } \mathbf{y}}{\sum_{\mathbf{y} \in \Theta_{\mathbf{x}}} \text{number of normal cells} + \text{number of cancer cells at site } \mathbf{y}}, \tag{A6}$$

where the neighbourhood $\Theta_{\mathbf{x}}$ is simply the cell's lattice site $\mathbf{x}$ if that site contains more than one cell, and otherwise Θ_i includes lattice sites in the Moore neighbourhood of $\mathbf{x}$.

At steady state, equation (A2) gives $[p53] = k_7(C_{p53} + C)/(k_7' C)$. Solving this for C, when $[p53] = p53_{THR}$, gives the approximate (bearing in mind that $[p53]$ is a dynamic variable) critical oxygen value for apoptosis as $C_{apo} = k_7 C_{p53}/(p53_{THR} k_7' - k_7)$. This relationship is used in Table S2 to link the parameter values for $p53_{THR}^{high/low}$ to equivalent oxygen thresholds for apoptosis.

Cancer cell apoptosis occurs if a cancer cell is quiescent for too long (when $T_{quiescent} > T_{death}$).

When a cell dies, it is removed from the computational domain.

A.2 Diffusible layer

In [45], diffusive transport of oxygen and VEGF within the tissue provides indirect coupling between the vascular and cellular layers. For both species, reaction-diffusion equations, at quasi-steady state, are used to model their spatio-temporal behaviour. We extend this approach to include quasi-steady equations for the concentrations of prodrug, P, and drug, Q. Hence the distributions of oxygen, VEGF, prodrug and drug are governed by equations of the form:

$$0 = D_u \nabla^2 U + \rho_v \psi_u (U_{blood} - U) + S_u - \delta_u U, \tag{A7}$$

where D_u is the diffusion coefficient of the species of interest in the extracellular space, $\rho_v(\mathbf{x}, t)$ is the vascular surface density at $\mathbf{x}$ in $\mathrm{cm}^2/\mathrm{cm}^3$, ψ_u is the vessel permeability to U, $U_{blood}(\mathbf{x}, t)$ is the concentration of U in the blood, $S_u(\mathbf{x}, t)$ is the cell- and environment-dependent production/removal rate and δ_u is the decay rate (see also equation (3) in the "Quick guide to equations and assumptions"). In all cases considered here, and for all diffusibles, we use zero flux boundary conditions.

We use a finite difference approximation, on the same lattice as the cells reside, to solve the quasi-steady elliptic equation (A7), with the vascular density at site $\mathbf{x}$ defined to be $\rho_v(\mathbf{x}, t) = 2\pi R(\mathbf{x}, t) L(\mathbf{x}, t)/\Delta x^3$ if a flowing vessel is present there, and zero otherwise. Here $R(\mathbf{x}, t)$ and $L(\mathbf{x}, t)$ are the vessel radius and length, so that $\rho_v(\mathbf{x}, t)$ is the surface area of a cylindrical vessel, divided by the lattice site volume (assuming the tissue thickness is Δx).

We note that for the production and uptake terms, $S_u(\mathbf{x}, t)$, cells and vessels may be sources or sinks of oxygen, VEGF, prodrug and drug. If there are two cancer cells at a site, each makes a contribution to oxygen consumption. Consequently, higher cell densities will lead to lower oxygen and hence reduced proliferation and increased rates of apoptosis/entry to quiescence.

A.2.1 Oxygen, C

Each branch of the vascular network acts as a distributed source of oxygen whereas the oxygen-consuming cells act as spatially-distributed sinks. Hence the oxygen concentration is described by equation (A7), with $C_{blood}(\mathbf{x}, t) = C_{ref} H(\mathbf{x}, t)/H_{in}$,

$$S_c(\mathbf{x}, t) = -\sum_{cell\ at\ \mathbf{x}} k_c^{cell} C, \tag{A8}$$

and $\delta_c = 0$. Here, C_{ref} is a reference oxygen concentration, $H(\mathbf{x}, t)$ is the haematocrit value in the vessel at position $\mathbf{x}$, and H_{in} the reference inflow haematocrit, so that for flowing vessels (and with symmetric haematocrit splitting at bifurcations) we have $C_{blood}(\mathbf{x}, t) = C_{ref}$.

Multiple cells at lattice site $\mathbf{x}$ at time t contribute to the consumption rate (each cell at rate k_c^{cell}), so that $S_c(\mathbf{x}, t)$ is a sum over all cells at $\mathbf{x}$. Hence a higher cell density at $\mathbf{x}$ gives a greater overall rate of oxygen consumption at that site.

A.2.2 VEGF, V

The vessels act as sinks and the cells as sources of VEGF. It is assumed that the level of VEGF in the blood is negligible.

VEGF is secreted by quiescent cancer cells, and by normal cells if their internal VEGF level satisfies $[VEGF] > V_{THR}$. The VEGF secretion rate is given by k_v^{cell}, which depends on the cell-type at $\mathbf{x}$. Hence, the VEGF distribution is specified by equation (A7), with $V_{blood} = 0$ and

$$S_v(\mathbf{x}, t) = \sum_{cell\ at\ \mathbf{x}} k_v^{cell}. \tag{A9}$$

We measure VEGF in nM, and consider a typical concentration to be 1 nM.

A.2.3 Prodrug, P

The prodrug concentration, P, is governed by equation (A7), where $P_{blood}(\mathbf{x}, t)$ and $S_p(\mathbf{x}, t)$ depend on the delivery and macrophage-dependent activation steps detailed in Section A.5.2 below.

A.2.4 Drug, Q

The drug concentration, Q, is governed by equation (A7), where $Q_{blood}(\mathbf{x}, t)$ and $S_q(\mathbf{x}, t)$ depend on the delivery method (conventional or macrophage-dependent). See Sections A.4 and A.5.2 below.

A.3 Vascular layer

A.3.1 Initialisation

The initial vessel network is specified by a set of inflow nodes (with associated pressures and haematocrits), outflow nodes (with associated pressures), and a set of vessel segments that connect neighbouring lattice sites. For all simulations, we specify the initial network as a pair of straight connections (each with 50 segments of length Δx): one connection from an inflow at lattice site $(1, 12)$ to an outflow at $(51, 12)$, and a second connection from $(1, 40)$ to $(51, 40)$.

A.3.2 Macrophage extravasation

See Section A.7 below.

A.3.3 Angiogenic tip cell sprouting

Angiogenesis is included by allowing endothelial sprouts to emerge from existing vessels with probability $Pr_{sprout}(\mathbf{x}, t)$ which is an increasing function of VEGF, and proportional to the vessel surface area at $\mathbf{x}$.

On each time step Δt, the probability of an endothelial tip cell sprouting from a vessel at lattice site $\mathbf{x}$ is

$$Pr_{sprout}(\mathbf{x}, t) = \Delta t 2\pi R(\mathbf{x}, t) L(\mathbf{x}, t) \frac{P_{sprout}^{max} V(\mathbf{x}, t)}{V_{sprout} + V(\mathbf{x}, t)}, \tag{A10}$$

where P_{sprout}^{max} is the maximum probability and V_{sprout} the VEGF concentration at which the probability is half-maximal [45]. If the number of cells at site $\mathbf{x}$ exceeds the carrying capacity for sprout emergence, E_m^{tipcell}, then the probability of a sprout emerging is set to zero. Similarly, $Pr_{sprout}(\mathbf{x}, t) = 0$ in the vicinity of another sprout (within a defined radius of exclusion, R_{ex}), since Delta-Notch signalling inhibits sprouts from forming in adjacent endothelial cells [33, 64].

If sprouting occurs, a new endothelial tip-cell is created at the relevant lattice site, and subsequently that tip cell performs a random walk, biased up VEGF concentration gradients, according to equation (A4). When a tip cell moves away from a site, a stationary endothelial cell is left behind [45]. Thus the sprout is extended without endothelial cell proliferation being explicitly modelled. This has been termed the "snail trail" approach, and is widely used in models for angiogenesis (see [34] and references therein).

A.3.4 Anastomosis

For blood flow to start within the sprout, anastomosis, or loop formation, must occur. Anastomosis is assumed to take place when a tip cell moves to a lattice site already occupied by a sprout or by a vessel [45]. If anastomosis does not occur within a given time, then the sprout dies and is removed, i.e. endothelial cells within newly formed sprouts must experience a flow stimulus to stay alive. The maximum sprout survival time without anastomosis is set to the time vessels can survive with low wall shear stress, T_{prune} (see A.3.5 below).

A.3.5 Vessel pruning

At each time step, Δt, vessel segments are pruned, due to low flow [17, 51], if their wall shear stress remains below a threshold value, τ_w^{crit}, for longer than a prescribed period, T_{prune} [45].

A.3.6 Calculate pressures, flows and vessel radii

The vessel radii vary in response to a variety of stimuli: the haemodynamic stimulus depends on the wall shear stress and intravascular pressure; the metabolic stimulus depends on the haematocrit and the flow; and the shrinking stimulus reflects the vessels' natural tendency to regress if positive stimuli are absent [45, 48]. After adaptation of the vessel radii, the blood flow is determined via the Poiseuille approximation and conservation of mass at each node, together with specified inflow and outflow pressures. Once the flows and the vessel radii have been determined, we prescribe, for simplicity, a haematocrit value equal to the inflow haematocrit (i.e. $H(\mathbf{x}, t) = H_{in}$) in vessel segments that sustain flow, and zero in segments lacking flow (i.e. $H(\mathbf{x}, t) = 0$). These haematocrit values are then used to update the vessel radii. Since the new values of the vessel radii and the haematocrit affect the flows, on each time step of a simulation, the calculation of flows, haematocrits and radii is iterated until the maximum proportional change in vessel radius across the network is less than a pre-determined value, R_{reltol} [45]. This approach reflects the assumption that the vessel radii, haematocrits and flows are at quasi-steady state with respect to the other layers of the multiscale model [45].

A.4 Conventional delivery of Cyclophosphamide

We assume that the prodrug cyclophosphamide is rapidly metabolised in the liver, from where the active drug re-enters the circulation at a concentration that is proportional to the blood plasma volume fraction, $(1 - H(\mathbf{x}, t))$. In addition, we assume that boluses of magnitude Q_{bolus} are applied

at times T_n^q, after which plasma levels decay exponentially, so that the active drug concentration in the bloodstream, $Q_{blood}(\mathbf{x}, t)$, is given by

$$Q_{blood}(\mathbf{x}, t) = \begin{cases} Q_{bolus}(1 - H(\mathbf{x}, t))e^{-k_{qc}(t-T_n^q)} & \text{for } T_n^q \leq t < T_{n+1}^q, \\ 0 & \text{otherwise.} \end{cases} \tag{A11}$$

where $H(\mathbf{x}, t)$ is the haematocrit value in the vessel at position $\mathbf{x}$.

The active drug enters the tumour tissue across the vessel walls and then diffuses and undergoes linear decay, so that the drug concentration in the tissue, $Q(\mathbf{x}, t)$, is governed by equation (A7) with Q_{blood} as defined in equation (A11) and $S_q \equiv 0$.

In the absence of specific *in vivo* data (see Table S7) we scale drug concentrations so that $Q_{crit} = 1$, and investigate the effect of a range of relative concentrations of applied drug. We use the same scaling for prodrug concentrations when considering macrophage therapy.

A.5 Macrophage-based gene therapy

Macrophages are white blood cells, which differentiate from precursors in the blood called monocytes, following monocyte extravasation into the tissue. Macrophage-based gene therapy aims to transfect a patient's own monocytes with a therapeutic gene, and use the ability of monocytes/macrophages to home in on hypoxic tissues.

As explained below, we model macrophage therapy by including the following processes: (1) monocyte adhesion to the endothelium and extravasation from blood into the tissue site, (2) movement in the tissue and (3) hypoxia-induced prodrug activation. We defer discussion of monocyte adhesion and extravasation to Section A.7.2, where we include the effect of a magnetic field on monocytes loaded with magnetic nanoparticles.

A.5.1 Macrophage movement

We simulate macrophage movement as a random walk, biased up gradients in VEGF, which acts as a chemoattractant for macrophages [7, 18]. We use the same form of movement probability as that used for tip cell movement in sprouting angiogenesis (see equation (A4)).

By comparing the magnitude of the force spontaneously generated by macrophages as they migrate through tissue (estimated to be 2-11 nN [29, 70]) with the magnetic force acting on the macrophages ($|\mathbf{F_{mag}}| = 2.40 \times 10^{-2}$ nN, as determined below), we find that the magnetic effect on movement can be neglected. Thus we assume that once the macrophages have extravasated their movement is no longer affected by the magnet.

A.5.2 Hypoxia-induced prodrug activation by macrophages

We assume that the prodrug is injected into the bloodstream in such a way that its concentration in the bloodstream, $P_{blood}(\mathbf{x}, t)$, is proportional to the blood plasma volume fraction, i.e.

$$P_{blood}(\mathbf{x}, t) = \begin{cases} P_{bolus}(1 - H(\mathbf{x}, t))e^{-k_{pc}(t-T_n^p)} & \text{for } T_n^p \leq t < T_{n+1}^p, \\ 0 & \text{otherwise.} \end{cases} \tag{A12}$$

where $H(\mathbf{x}, t)$ is the haematocrit in the vessel at position $\mathbf{x}$. The prodrug enters the tumour tissue across the vessel walls and then diffuses and decays. When the prodrug comes into contact with

hypoxic macrophages (i.e. macrophages at locations with a tissue oxygen level below a threshold, $C(\mathbf{x},t) < C_{hyp}$) the prodrug is converted, with rate constant k_{pq}, into active drug.

Once active drug has been produced, it diffuses and decays so that the drug concentration, Q, in the tissue at quasi-steady state is given by equation (A7) with $Q_{blood} \equiv 0$ and

$$S_q(\mathbf{x},t) = \begin{cases} k_{pq}P(\mathbf{x},t) & \text{if a Macrophage is at } \mathbf{x} \text{ and } C(\mathbf{x},t) < C_{hyp}, \\ 0 & \text{otherwise.} \end{cases} \tag{A13}$$

The concentration of prodrug in the tissue, $P(\mathbf{x},t)$, therefore satisfies equation (A7) with P_{blood} as defined in equation (A12) with $S_p(\mathbf{x},t) = -S_q(\mathbf{x},t)$.

The prodrug concentration has the same scaling as active drug, with 1 unit corresponding to the critical tissue concentration for drug intercalation.

A.6 Cytotoxic drug action

If $Q(\mathbf{x},t) > Q_{crit}$ then any cell at site $\mathbf{x}$ intercalates active drug. Cells with drug intercalated die upon attempting cell-division (so this only applies to normal and cancer cells). This applies to both conventional and macrophage-based drug delivery.

A.7 Enhancing macrophage therapy via magnetic nanoparticles

A.7.1 Magnetic field and magnetic velocity of the macrophages

In the blood stream the net velocity of the macrophages is the sum of the fluid velocity, $\mathbf{v_{blood}}$, and the velocity due to the magnetic field, $\mathbf{v_{mag}}$ [30]. In our multiscale model $\mathbf{v_{blood}}$ is determined from the flow calculation described above. For a macrophage of radius r_m the magnetic velocity is given by

$$\mathbf{v_{mag}} = \frac{\mathbf{F_{mag}}}{6\pi\mu r_m}, \tag{A14}$$

where μ is the dynamic viscosity of the fluid and $\mathbf{F_{mag}}$ is the magnetic force on the macrophage [30]. The magnetic force is given by

$$\mathbf{F_{mag}} = \frac{|\mathbf{m}|(\mathbf{B}\cdot\nabla)\mathbf{B}}{|\mathbf{B}|}, \tag{A15}$$

where $\mathbf{B}$ is the magnetic field and $\mathbf{m}$ is the magnetic moment of the particle [30]. The magnetic moment is in turn given by

$$\mathbf{m} = \frac{m_{sat}\mathbf{B}L(|\mathbf{B}|)}{|\mathbf{B}|}, \tag{A16}$$

where

$$L(|\mathbf{B}|) = \coth(\epsilon|\mathbf{B}|) - \frac{1}{\epsilon|\mathbf{B}|}, \tag{A17}$$

and

$$\epsilon = \frac{m_{sat}}{kT}, \tag{A18}$$

where m_{sat} is the saturation magnetisation of the magnetic particle, k is the Boltzmann constant and T is the absolute temperature (measured in Kelvin) [30]. To obtain m_{sat} we use the following relation:

$$m_{sat} = \frac{4}{3}\pi r_m^3 M_{sat}\rho\xi, \tag{A19}$$

where M_{sat} is the typical saturation value of macrophage mass magnetisation, ρ is the density of magnetite and ξ is the proportion of magnetite by macrophage volume.

We consider the magnetic field to be constant throughout the small tumour region that we simulate. Furthermore, we assume that the magnetic field corresponds to the on-axis field above a circular current-carrying loop centered at the origin in the xy-plane. The magnetic field on the z-axis at a distance z above a current loop is given by

$$\mathbf{B} = \frac{\mu_0 I r_c^2 \hat{\mathbf{z}}}{2(r_c^2 + z^2)^{3/2}}, \tag{A20}$$

where μ_0 is the permeability of free space, I is the current counter-clockwise in the xy-plane, r_c is the radius of the circular current loop and $\hat{\mathbf{z}}$ is the unit-vector pointing in the positive z-direction. With the parameter values in Table S8, from formula (A20) we obtain $|\mathbf{B}| = 0.1302$ NA^{-1}m^{-1}, which is the value we use in all our simulations. Between simulations we only vary the direction of $\mathbf{B}$, i.e. the macrophages always experience the same magnetic speed.

For the parameters under consideration here, $\epsilon|\mathbf{B}| \gg 1$ and hence we use the approximation $L(|\mathbf{B}|) = 1$ so that formula (A16) reduces to

$$\mathbf{m} = \frac{m_{sat}\mathbf{B}}{|\mathbf{B}|}. \tag{A21}$$

Substituting equations (A15), (A20) and (A21) into (A14) we obtain

$$\mathbf{v_{mag}} = \frac{-3 m_{sat} \mu_0 I r_c^2 z \hat{\mathbf{z}}}{12(r_c^2 + z^2)^{5/2} \pi \mu r_m}. \tag{A22}$$

Using (A22) with the parameter values in Table S8, the magnetic speed is $|\mathbf{v_{mag}}| = 7.08 \times 10^{-5}$ m/s, which according to equation (A15) corresponds to a magnetic force of $|\mathbf{F_{mag}}| = 2.40 \times 10^{-11}$ N acting on the macrophages.

A.7.2 Adhesion and extravasation of macrophages

We assume a single injection of macrophages into the blood, at time T_{mac}, with a clearance rate chosen to match approximately the observed uptake within 5 hours of magnetically loaded macrophages in mice [44]. In addition, we assume that $M_{blood}(\mathbf{x}, t)$, the concentration of magnetic macrophages in a vessel segment at position $\mathbf{x}$, is proportional to the haematocrit in that segment, $H(\mathbf{x}, t)$, so that

$$M_{blood}(\mathbf{x}, t) = k_M \frac{H(\mathbf{x}, t)}{H_{in}} e^{-k_{mac}(t - T_{mac})}, \tag{A23}$$

implying that macrophages split in the same way as red blood cells and other cellular components of blood. For simplicity we view adhesion of macrophages to the tumour endothelium and their subsequent extravasation as a single, composite process. The probability of extravasation is the sum of an intrinsic component (characterised by the parameter α_m) and a contribution due to the magnetic field (whose strength is characterised by the parameter β_m). Following [30] we assume that the magnetic contribution is given by $\beta_m|\mathbf{v_{mag}} \cdot \mathbf{n}(\mathbf{x}, t)|$ where β_m is a constant characterising the strength of the magnetic contribution, and $\mathbf{n}(\mathbf{x}, t)$ is the unit vector normal to the vessel wall. Since macrophage adhesion increases with VEGF levels [18], we assume that the sum of normal and magnetic extravasation is multiplied by a saturating function of the local VEGF concentration, $V(\mathbf{x}, t)$. In addition we assume that the total extravasation is proportional to the surface area of the vessel segment, and its macrophage concentration, $M_{blood}(\mathbf{x}, t)$, so that on one timestep Δt the probability of adhesion and extravasation from a vessel segment at $\mathbf{x}$, $Pr^{\text{mac}}_{\text{extra}}(\mathbf{x}, t)$, is given by

$$Pr^{\text{mac}}_{\text{extra}}(\mathbf{x}, t) = \Delta t 2\pi R(\mathbf{x}, t) L(\mathbf{x}, t) M_{blood}(\mathbf{x}, t) \frac{V(\mathbf{x}, t)}{A_v + V(\mathbf{x}, t)} (\alpha_m + \beta_m |\mathbf{v_{mag}} \cdot \mathbf{n}(\mathbf{x}, t)|), \tag{A24}$$

where A_v is the VEGF concentration at which the rate of extravasation is half-maximal. Extravasation can only occur if there is sufficient space at lattice site $\mathbf{x}$ ($N_{\mathbf{x}} < E_m^{\text{mac}}$ where E_m^{mac} is the carrying capacity for macrophage extravasation). Tissue macrophages do not proliferate, and have a normally distributed survival time (mean $\mu_{\text{lifespan}}^{\text{mac}}$, standard deviation $\sigma_{\text{lifespan}}^{\text{mac}}$).

B Computational details and timing

The model is implemented in C++, using CVODE [56] to integrate the subcellular ODEs, and SuperLU [19] to solve the linear systems for the flow calculation and reaction diffusion equations. We use the Mersenne Twister algorithm to generate the different sequences of random numbers that give each computational realisation for a given parameter set [67].

Each simulation took approximately 1 hour to run on Dell PowerEdge R610 servers with two Intel Xeon X5570 processors (8 processor cores total), and we typically ran up to six simulations at a time. The figures in the main manuscript represent the results of 380 simulations (10 realisations for each of 38 cases), and the figures in the supplement represent a further 240 simulations.

C Parameter values

Parameters used throughout the manuscript are listed in tables S1–S8, along with a description of their meaning, comments and relevant references. Where possible, we use parameter values based on published data, and choose other parameter values that give physiologically realistic behaviours (e.g. tissue gradients, ratio of drug to prodrug). We explore the sensitivity to various parameters, particularly the therapeutic inputs (Q_{bolus} for conventional therapy, and P_{bolus} for macrophage therapy), but it is not possible to carry out a full sensitivity study. By focusing on the behaviour close to the EC50s for treatment efficacies, we are able to concentrate on the similarities and differences between therapeutic modes of action, and possible synergies between them.

Table S1 includes the domain size, time step, and parameters that only apply to normal cells. Table S2 includes parameters that are defined for both normal and cancer cells (in particular for the new cell cycle phase model), and Table S3 has parameters that are specific to cancer cells. Table S4 includes parameters that differ between the four cell types involved (normal cells, cancer cells, endothelial cells and macrophages) and hence includes the parameters that govern macrophage movement. Table S5 includes parameters for diffusibles, Table S6 has vascular parameters, Table S7 includes parameters for macrophage-based gene therapy, and Table S8 includes parameters for the effect of a magnetic field on macrophages loaded with magnetic nanoparticles.

Parameter	Default value	Meaning, references & comments
Δt	30 min	Time step between Cell, Diffusible and Vascular updates.
Δx	40 μm	Lattice site dimension.
Domain size	51×51 sites	Corresponds to a parent vessel length of 2mm (same as in modelling of [42]), and a domain size of 2.04mm $\times$ 2.04mm.
T_{final}	200 days	Total duration of all simulations (except for simulations of macrophage infiltration with and without a magnetic field, Fig 6, which were run for 7 days).
$[VEGF]_0$	0.0	Initial intracellular VEGF concentration [3] ($*_1$).
$[p53]_0$	0.0	Initial intracellular p53 concentration ($*_1$).
k_7	0.002 min^{-1}	Intracellular p53 production [3] ($*_1$).
$k_7^{'}$	0.01 min^{-1}	Maximum rate of intracellular p53 degradation [3] ($*_1$).
C_{p53}	0.01 (4.44 mmHg)	Tissue oxygen concentration for half-maximal intracellular p53 degradation [3] ($*_1$).
k_8	0.002 min^{-1}	Basal intracellular VEGF production [3] ($*_1$).
$k_8^{''}$	-0.002 min^{-1}	Effect of p53 on VEGF production [3]. In normal cells p53 inhibits VEGF production [54] ($*_1$).
J_5	0.04	Intracellular VEGF for half-maximal VEGF-dependent intracellular VEGF production [3] ($*_1$).
$k_8^{'}$	0.01 min^{-1}	Maximum rate of intracellular VEGF degradation [3] ($*_1$).
C_{VEGF}	0.01 (4.44 mmHg)	Tissue oxygen concentration for half-maximal intracellular VEGF degradation [3] ($*_1$).
ρ_{THR}	0.75	Threshold of ratio of normal to tumour cells for altered p53 response. This value means that any normal cell sharing a lattice site with a cancer cell will undergo apoptosis (see comments for the parameter $p53_{THR}^{low}$).
$p53_{THR}^{high}$	0.8	$[p53]$ threshold for apoptosis of normal cells. When the p53-VEGF system is at steady state, this corresponds to oxygen at 1.5mmHg (severe hypoxia [36]).
$p53_{THR}^{low}$	0.08	$[p53]$ threshold for apoptosis of normal cells in a tumour microenvironment. When the p53-VEGF system is at steady state, $[p53] > p53_{THR}^{low}$ for all oxygen concentrations, so that apoptosis is triggered in any normal cell in such a microenvironment. The value chosen corresponds to this modelling assumption, and is identical to that used in [3, 45].
V_{THR}	0.27	Internal VEGF threshold for VEGF release. Corresponds to VEGF release at hypoxic oxygen levels of 3.8mmHg. This is equal to 0.5% oxygen, found to induce maximal expression of Hypoxia-Inducible Factor 1 (HIF1), which leads to the expression of VEGF [36].

Table S1: Parameters for the multiscale model, common to the whole simulation, and parameters for normal cells only. Cell-cycle parameters, for the phase model (A1), are given in Table S2. $*_1$: The p53-VEGF model is dimensionless, and its parameters are chosen to stimulate apoptosis and VEGF release at physiologically realistic oxygen levels [36]. To the best of our knowledge, there is no experimental data that would allow more detailed calibration of the parameters for this sub-model.

Parameter	Normal cell	Cancer cell	Meaning, references & comments
D_m	1	2	Carrying capacity for cell division. We assume that cancer cells can tolerate a higher cell density.
C_ϕ	3 mmHg	1.4 mmHg	O_2 for half maximal cell cycle rate in equation (A1). These were chosen to fit with previous modelling [2]. For comparison, Casciari *et al.* [14] find that the oxygen concentration for half maximal proliferation rate is 7.3×10^{-3}mM. This corresponds to approximately 5 mmHg.
$T_{\min}$	3000 min	1600 min	Minimum cell cycle times (48 hours for normal cells, 27 hours for cancer cells). These were chosen to fit with previous modelling [2], and are consistent with many cell types.
k_v^{cell}	0.01 nM/min	0.01 nM/min	VEGF release rate (where *cell* indicates the cell type). We measure VEGF in nM, and consider a typical concentration to be 1 nM. Akeson *et al.* studied endothelial cell (EC) activation by VEGF from 0 to 2.38 nM, and found half-maximal VEGF Receptor 2 (VEGFR2) phosphorylation at 0.65 nM [1]). These values are consistent with other studies of responses to VEGF [25, 66]. Given a decay rate of $\delta_v = 0.01$/min (see below), this means the maximum production rate should be $0.01 \times 2.38nM/\text{min} = 0.0238nM/\text{min}$.

Table S2: Parameter values for processes common to normal and cancer cells. Includes parameters relating to the cell cycle model, equation (A1).

Parameter	Cancer cell	Meaning, references & comments
$C^{\text{enter}}_{\text{quiesc}'}$	8.9 mmHg	O_2 for entering quiescence. This level corresponds to weak hypoxia, and gives quiescent tumour cell fractions of approximately 10%. Derived from the [$p27$] threshold ($p27_e$) assumed in the model of Owen *et al.* [45].
$C^{\text{leave}}_{\text{quiesc}'}$	9.8 mmHg	O_2 for leaving quiescence. 10% larger that the value for $C^{\text{enter}}_{\text{quiesc}'}$. This level corresponds to weak hypoxia, and gives quiescent tumour cell fractions of approximately 10%.
T_{death}	4000 min	Time a cancer cell can remain quiescent for. Hypoxic human tumour cells remained viable for 3–10 days in xenografts and spheroids, and hypoxic rodent cells remained viable for 1–3 days in spheroids [23].

Table S3: Parameter values for cancer cells only — for entry to and exit from quiescence, and apoptosis.

Param'	Normal Cell	Cancer Cell	EC / Tip Cell	Macro-phage	Meaning, references & comments
k_c^{cell}	13	13	13	13	O_2 consumption (min^{-1}): *cell* indicates cell type. For simplicity, we use equal rates except for functional vessels ($k_c^{vessel} = 5/\text{min}$). Many authors use Michaelis-Menten kinetics for oxygen uptake, of the form $M_0 C/(C + P_0)$ [28, 55]. To keep the elliptic equations (A7) linear, we consider the form $S_c(\mathbf{x}, t) = -\sum k_c^{cell} C$, with $k_c^{cell} \sim M_0/(C^* + P_0)$ for typical tissue oxygen concentrations C^*. In [55], $M_0 = 2\text{cm}^3\text{O}_2/100\text{g/min} \approx 514\text{mmHg/min}$, and $P_0 = 1\text{mmHg}$. At $C^* = 20 mmHg$ this gives $k_c^{cell} \sim 514/21 = 24.5/\text{min}$. In [28], $M_0 = 1.57 \times 10^{-4}\text{ml O}_2/\text{ml/s} = 242\text{mmHg/min}$, and $P_0 = 0.5\text{mmHg}$. At $C^* = 20 mmHg$ this gives $k_c^{cell} \sim 242/20.5 = 11.8/\text{min}$.
D	0	0.5	1.0	1.0	Random motility ($\mu\text{m}^2/\text{min}$). We neglect movement of normal cells (in the model they spread via cell division, since their carrying capacity, $N_m = 1$). For animal cells, Bray estimated $D = 3\mu\text{m}^2/\text{min}$ [11]. In various models for wound healing *in vivo*, Sherratt and Murray estimate $D = 0.41$–$18\mu\text{m}^2/\text{min}$ [57]. For endothelial cells *in vitro*, Stokes *et al.* find $D = 42.6\mu\text{m}^2/\text{min}$ [61]. Kouvroukoglou *et al.* [39] studied EC migration on different surfaces and found $D = 5.83$–$19.2\mu\text{m}^2/\text{min}$. Anderson & Chaplain use $D = 0.6\mu\text{m}^2/\text{min}$ [4]. For macrophages, Owen & Sherratt estimate $D = 0.28$–$0.624\mu\text{m}^2/\text{min}$ [46].
χ	0	0	2×10^4	2×10^4	Chemotaxis coefficient ($\mu\text{m}^2/\text{min/nM}$). Stokes & Lauffenberger [62] give $\chi = 1.56 \times 10^4 \mu\text{m}^2/\text{min/nM}$, for microvessel endothelial cells in gradients of acidic FGF. Concentrations were about 0.1nM, similar to our characteristic VEGF concentration (see V_{sprout}). For macrophage chemotaxis *in vitro* in response to MCP-1, Owen & Sherratt estimate $\chi = 0.12$–$0.37 \times 10^4 \mu\text{m}^2/\text{min/nM}$. We used chemotaxis coefficients with a similar order of magnitude.
N_m	1	2	3	4	Carrying capacity for cell movement ($*_2$).
$E_m^{tipcell}$	–	–	3	–	Carrying capacity for tip cell sprouting ($*_2$).
E_m^{mac}	–	–	–	4	Carrying capacity for macrophage extravasation ($*_2$).
P_{sprout}^{max}	–	–	0.00025	–	Maximum rate of endothelial sprouting (min^{-1}). Set to give normal tissues with appropriate vascular density.
V_{sprout}	–	–	0.5	–	VEGF for half-maximal tip-cell sprouting (nM), corresponding to the EC50 for VEGFR2 activation by VEGF [1].
R_{ex}	–	–	$2\Delta x$	–	Exclusion radius for tip cell emergence. Angiogenic sprouts are inhibited from forming in adjacent endothelial cells [33, 64].

Table S4: Parameters for all cell types, where a dash indicates a parameter that is not defined for that cell type. $*_2$: $E_m^{tipcell}$ and $N_m^{tipcell}$, are one more than N_m^{cancer}, in order to allow endothelial tip cells to sprout within and move to sites already occupied by cancer cells. For similar reasons, we prescribe E_m^{mac} and N_m^{mac} to be one more than the corresponding values for endothelial cells.

Parameter	Default value	Meaning, references & comments
D_c	0.00145 cm^2/min	Oxygen diffusion [8, 28].
D_v	10^{-5} cm^2/min	VEGF diffusion. This is approximately 6-fold smaller than the value used in [41], and the value predicted from the VEGF molecular weight (45000) using the formula in [10]. This reduction accounts for binding to ECM [9]. The value used is also similar to that of 6×10^{-6} cm^2/min for *typical angiogenic factor diffusion* in [63].
D_p	10^{-4} cm^2/min	Prodrug diffusion coefficient. Cyclophosphamide molecular weight is 261 (279 in hydrated form), for which the formula in [10] gives 3.2×10^{-4} cm^2/min. However, glucose has a similar molecular weight (MW 180) and has an estimated diffusion coefficient in tumour spheroids of 0.6×10^{-4} cm^2/min [13]. This is similar to the value of 0.96×10^{-4} cm^2/min used in a model for Doxorubicin (MW 544) [24].
D_q	10^{-4} cm^2/min	Drug diffusion coefficient, assumed to be similar to that for prodrug (D_p). The primary active metabolite of cyclophosphamide is 4-hydroxycyclophosphamide (4-HO-CP), which has a similar molecular weight.
ψ_c	6 cm/min	Vessel permeability to Oxygen. Goldman & Popel use a mass transfer coefficient of $k = 4\times10^{-6}$mlO$_2$/s/mmHg/cm^2 [28]. This is converted to cm/min by dividing k by the tissue oxygen solubility $\alpha = 3.89\times10^{-5}mlO_2$/ml/mmHg, and multiplying by 60.
ψ_v	10^{-5} cm/min	Vessel permeability to VEGF. Stefanini *et al.* use 0.24×10^{-5}cm/min and 2.4×10^{-5}cm/min for normal and tumour tissue [60]. This value is also consistent with those used for Prodrug (ψ_p) and Drug (ψ_q).
ψ_p	10^{-4} cm/min	Vessel permeability to Prodrug. Cyclophosphamide molecular weight is 261 (279 in hydrated form), so we expect a greater permeability than for sulforhodamine (MW = 558), which has a permeability in granulating tissue of 3.4×10^{-5}cm/s [69]. This value is also consistent with those used for VEGF (ψ_v) and Drug (ψ_q).
ψ_q	10^{-4} cm/min	Vessel permeability to Drug. The primary active metabolite of cyclophosphamide is 4-hydroxycyclophosphamide, which has a similar (slightly larger) molecular weight. Hence we use the same value as for Prodrug (ψ_p). This value is also consistent with that used for VEGF (ψ_v).
C_{ref}	20 mmHg	Reference oxygen tension in perfused vessels with reference haematocrit ($H(\mathbf{x},t) = H_{in}$). This gives perivascular oxygen of approximately 20mmHg, consistent with [37].
δ_v	0.01 min^{-1}	VEGF decay. The basal steady state VEGF concentration and basal production rate in Mac Gabhann *et al.* [41] require a decay rate of $\delta_v = 0.0105\text{min}^{-1}$. A fit of $dV/dt = p - \delta_v V$ to VEGF production time-course data gives $\delta_v = 0.0058$ (where $p = 0.0024$ng/gtissue/min is a constant production rate) [58].
δ_p	0.1	Prodrug decay rate in tissue. We are not aware of data on the decay and/or uptake of interstitial (as opposed to blood) cyclophosphamide.
δ_q	0.1	Drug decay rate in tissue. We are not aware of data on the decay and/or uptake of interstitial (as opposed to blood) 4-hydroxycyclophosphamide.

Table S5: Parameters for the diffusible substances, Oxygen, VEGF, prodrug and drug: here we list diffusion coefficients, vascular permeabilities and decay rates. Oxygen consumption rates can be found in Table S4, VEGF production rates in Table S2, and parameters governing drug/prodrug delivery and prodrug activation in Table S7.

Parameter	Default value	Meaning, references & comments
P_{in}	25 mmHg	Inflow pressure (at all inflow nodes)
P_{out}	15 mmHg	Outflow pressure (at all outflow nodes)
H_{in}	0.45	Inflow Haematocrit (at all inflow nodes)
μ_{plasma}	0.72 g cm min^{-1}	Plasma viscosity [27].
k_s	1.7 s^{-1}	Shrinking tendency [48]
k_p	0.5 s^{-1}	Sensitivity to intravascular pressure [50].
k_m^0	1.7 s^{-1}	Metabolic stimulus [50].
k_m^V	0.0	VEGF-dependent part of metabolic stimulus.
V_0	10^{-3}	VEGF for half-maximal enhanced vessel dilation.
τ_{ref}	0	to avoid singular behaviour at low wall shear stress [48].
$\dot{Q}_{ref}$	4×10^{-5} cm^3 min^{-1}	reference flow rate for metabolic stimulus [50]
ϵ_t	0.1 s	Time step for updating vessel radii.
R_{reltol}	10^{-4}	Relative error tolerance for convergence in vascular adaptation.
R_{MIN}	1 μm	Minimum possible vessel radius.
R_{MAX}	50 μm	Maximum possible vessel radius.
τ_w^{crit}	8 dynes cm^{-2}	Critical wall shear stress for pruning. WSS in rat mesentery capillaries ranges from about 10 to 100 dynes cm^{-2} [49]. Mean WSS in conjunctival microvessels is 15.4 dynes cm^{-2} [38].
T_{prune}	4000 min	Critical duration of low wall shear stress for pruning. [43] suggest that there is some period of time for which there is minimal impact on capillary regression, up to some threshold. However, there is no indication of the relevant timescale. Vessel regression in the mouse eye [12], and tadpole tail [17], appears to take place over a period of days.

Table S6: Vasculature parameters, as described in [45].

Parameter	**Value**	Meaning, references & comments
k_{pc}	0.00048135 min^{-1}	Rate of Prodrug clearance from blood (half life of one day). This is in the range of reported values for drugs such as Cyclophosphamide [5, 15, 21] and Doxorubicin [22, 52].
k_{qc}	0.00048135 min^{-1}	Rate of Drug clearance from blood (half life of one day), assumed to be similar to Prodrug.
T_n^p	$21, 28, 35, \cdots, 147, 154$ days	Times of Prodrug injections. Such regular treatments have been used for a variety of drugs, e.g. [16]. Prodrug is only applied, according to equation (A12), for macrophage-based and combination therapies.
P_{bolus}	variable	Concentration of Prodrug injections (dimensionless).
T_n^q	$21, 28, 35, \cdots, 147, 154$ days	Times of active Drug delivery. Drug is only applied, according to equation (A11), for conventional and combination therapies.
Q_{bolus}	variable	Concentration of Drug injections (dimensionless).
C_{hyp}	3.8 mmHg	Oxygen threshold for prodrug activation by macrophages. This corresponds to 0.5% oxygen, coincident with maximal HIF1 expression [36]. This is also the oxygen concentration at which the steady state of the subcellular p53-VEGF model, equations (A2,A3), gives VEGF release from normal cells (i.e. when $[VEGF] = V_{THR}$).
k_{pq}	1min^{-1}	Rate constant for prodrug activation by macrophages. Pharmacokinetic data is available for cyclophosphamide (CP) [5, 15], but not for activation by transfected macrophages. For macrophage-therapy simulations, the rate used here gives ratios of drug to prodrug consistent with observed blood concentrations — e.g. in [5] the concentration of 4-HO-CP/AP (the active metabolite of CP) is 1-2 orders of magnitude smaller than that of CP. For $P_{bolus} = 120$, the ratio of Drug to Prodrug across the tissue averages approximately 0.07 over the duration of macrophage therapy, approx 0.05 for the larger prodrug dose of $P_{bolus} = 250$.
Q_{crit}	1.0	Threshold drug concentration for cell kill. Lee *et al.* studied active drug action, and found dose-dependence to vary between cell lines—the H226 lung cell line gave almost complete elimination for 10μM 4-HO-CP, whereas other cell lines required 100μM or more [40]. In the absence of specific *in vivo* data we scale drug and prodrug concentrations so that $Q_{crit} = 1$, and investigate the effect of a range of relative concentrations of applied prodrug/drug.

Table S7: Parameters relating to prodrug and drug delivery, and prodrug activation by hypoxic macrophages.

Parameter	Value	Meaning, references & comments
k_M	10^6 cells/cm^3	Typical macrophage concentration injected. Muthana *et al.* injected 3×10^6 human monocytes [44], and a typical mouse blood volume is 2cm^3.
T_{mac}	21 days	Time of injection of Macrophages. Macrophages are only applied, according to equation (A23), for macrophage-based and combination therapies.
k_{mac}	0.01155 min^{-1}	Rate of Macrophage clearance from blood (half life of one hour). This is consistent with observations that most human monocytes extravasate into tissues within 24 h of circulation in the bloodstream [53], and many are trapped in the lungs within 1 h [6].
$\mu^{\text{mac}}_{\text{lifespan}}$	90 days	Mean lifespan of macrophage in tissue [31, 53].
$\sigma^{\text{mac}}_{\text{lifespan}}$	9 days	Standard deviation of macrophage lifespan. Assumed.
A_v	0.5 nM	VEGF for half-maximal macrophage extravasation, corresponding to EC50 for VEGFR2 activation by VEGF [1]. [20] shows that macrophage infiltration can be mediated via VEGFR2.
α_m	0.00185 cm min^{-1}	Maximal effective vessel permeability to non-magnetic macrophages, fit to data from [44].
β_m	0.02528	Coefficient of magnetic enhancement of macrophage extravasation, fit to data from [44].
μ	3×10^{-3} N s m^{-2}	Dynamic viscosity of blood [30].
r_m	6×10^{-6} m	Monocyte/macrophage radius. Reported values for blood monocytes include 6.25μm for U937 cells, 8μm for Mono Mac 6 cells [26].
μ_0	$4\pi \times 10^{-7}$ NA^{-2}	Permeability of free space.
I	3.4752×10^4 A	Current in magnetic coil.
r_c	0.015 m	Radius of current loop.
z	0.03 m	Distance from current loop to tumour.
M_{sat}	50 Am^{2}kg^{-1}	Saturation value of macrophage mass magnetisation [30].
ρ	5.1×10^3 kgm^{-3}	Density of magnetite [30].
ξ	0.01	Proportion of magnetite by macrophage volume.
m_{sat}	2.3072×10^{-12} Am^2	Saturation magnetisation of the magnetic particle. Equation (A19).
$\lvert\mathbf{v_{mag}}\rvert$	7.08×10^{-5}/s	Component of magnetic monocyte speed due to magnetic field, from equation (A22).

Table S8: Parameters relating to macrophage delivery, lifespan in the tissue, and extravasation (including enhancement by magnetic nanoparticles).

D Supplementary results and figures

D.1 Validation

Here we focus on the underlying vascular tissue model, and show that the vascular networks generated by the multiscale model are consistent with data from the literature.

One measure of vascular density is surface area per unit volume of tissue. Grunstein *et al.* give vascular densities of 214 cm^2/cm^3 in mouse fibrosarcomas, and 36 cm^2/cm^3 in mouse fibrosarcomas that do not express VEGF [32]. For renal tissue, Köhler *et al.* find vascular densities of 115 cm^2/cm^3 (normal cortical renal parenchyma), 76 cm^2/cm^3 (normal medullary renal tissue), and 35–121 cm^2/cm^3 for renal tumours. For skeletal muscle, a vascular density of 130 cm^2/cm^3 has been reported [35].

For our model, it is straightforward to calculate the total surface area of vessels in the tissue domain, using the length and radius of each vessel segment. To divide by the appropriate volume, we assume that the tissue thickness is $\Delta x = 0.004$cm. In our simulations we obtained the following average vascular densities: normal tissue, 99 cm^2/cm^3; 21 day tumours, 146 cm^2/cm^3; developed tumours (at 200 days), 192 cm^2/cm^3. These values are consistent with the above experimental observations.

An alternative measure of vascular density is to count vessels per unit area in 2D sections. Srivastava *et al.* give 5900 vessels/cm^2 in non-metastatic melanomas (4200 vessels/cm^2 in normal dermis); and 7160 vessels/cm^2 in metastatic melanomas (3100 vessels/cm^2 in normal dermis) [59]. Weidner *et al.* determined vascular densities in breast carcinoma: 9019 vessels/cm^2 (non-metastatic); 19629 vessels/cm^2 (metastatic)[68]. These values are in a similar range to those of [59], and suggest a higher vascular density in more invasive tumours.

This measure relies on most vessels passing through the tissue section, rather than running parallel to it, as they do for simulations in a two-dimensional domain. Nevertheless, it is informative to calculate this measure based on the number of vessel segments per unit area. For normal tissue, we have an average of 532 vessel segments in an area of 0.0416cm^2, which gives 12784 vessels/cm^2. For tumour tissue, we find 18601 vessels/cm^2 (after 21 days) and 23741 vessels/cm^2 (after 200 days). These are rather larger than the above experimental figures, but they are of the right order of magnitude, and the relative difference between normal and tumour tissue is about right. These discrepancies are most likely an artifact of the 2D nature of our simulations (in even a thin 3D slab, we would expect a lower vessel count, due to vessel paths moving above and below any particular cross-section).

In human conjunctival microvessels, blood flow ranged from 0.3 to 27.2 nL/min, with a mean of 6.2 nL/min, and wall shear stress ranged (WSS) from 0.28 to 95.5 dynes/cm^2 with a mean WSS of 15.4 dynes/cm^2 [38]. In rat mesentery, flow speeds in capillaries and venules are approximately 1mm/s, which, for a 14 μm diameter capillary, gives a volume flow rate of about 37 nL/min [49]. Flow speeds in arterioles range from 1 to 8 mm/s, and WSS ranges from about 10 to 100 dynes cm^{-2} [49].

For our normal tissue simulations, the mean flow rate is 31 nL/min, the mean speed is 1.45 mm/s and the mean WSS is 20.7 dynes/cm^2. The corresponding figures for tumours at day 21 (day 200) are: 25.3 nL/min (28.9 nL/min); 1.18 mm/s (1.34 mm/s); and 16.4 dynes/cm^2 (18.6 dynes/cm^2).

Measures such as the vascular density and flow are emergent, depending on many features of the model such as cell proliferation and VEGF production, endothelial cell chemotaxis, nutrient diffusion and consumption, vessel pruning, vessel-radii adaptation, etc. The above observations give us confidence that the underlying vascular tissue model provides a sound foundation for our study of conventional and macrophage-based therapies for cancer.

D.2 Supplementary figures

Here we present supplementary figures that are referred to in the main text.

Figure S4 reproduces in colour Figure 4 of the main text, with the time courses for each of ten simulations plotted in a different colour.

Figure S5 shows an additional example of time courses, for conventional therapy with $Q_{bolus} = 11$, macrophage therapy with $P_{bolus} = 120$, and their combination. This corresponds to the "drug", "mac" and combined "drug / mac" data in Figure 7 of the main text. Individually, conventional and macrophage therapy have a weak effect on the tumour, but when combined, the tumour is eliminated in 6/10 cases. This example highlights the variability between simulations.

Figure S6 illustrates similar features to those shown in Figure 7 of the main text, but with different drug and prodrug doses, and combinations thereof. This reinforces the synergistic benefit of combination therapy, and shows that the dependence on timing is robust.

To check the effect of the cell cycle speed on our results, we carried out simulations in which cancer cells cycled twice as fast. In this case, shown in Figure S7, conventional therapy is slightly less effective, whereas macrophage therapy is slightly more effective, and combination therapy is markedly more effective (the tumour is eliminated in 10/10 simulations, rather than 6/10) .

D.3 Altered computational order

In the model, the various processes are updated sequentially. However, the order of processing does not make a significant difference to the overall results. To demonstrate this, we carried out simulations with an altered ordering, across the full range of the conventional dose-response curve. The standard ordering is indicated in Figure S2, and we altered this by carrying out the vascular update first, swapping the positions of oxygen and VEGF updates, and changing the order of cell movement and cell division. The altered ordering is indicated in a modified flowchart in Figure S8A. Illustrative results, presented in Figure S8B, show that the qualitative and quantitative dose response is insensitive to changes in the order of processing.

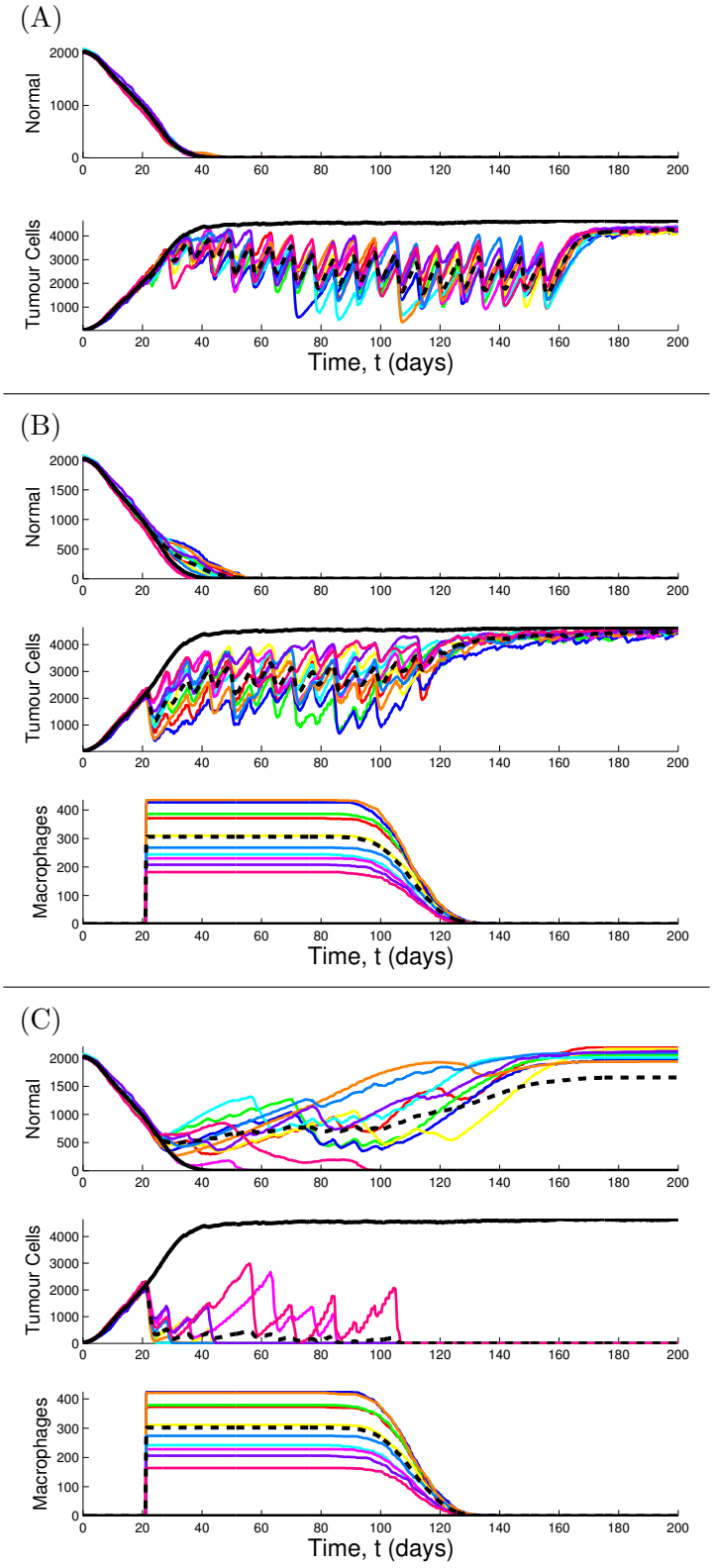

Figure S4: **Colour version of Figure 4:** The response to therapy over time. **(A)** Conventional therapy, $Q_{bolus} = 12$. Each bolus leads initially to tumour regression and then regrowth. **(B)** Engineered macrophages accumulate after injection on day 21. Weekly prodrug boluses ($P_{bolus} = 250$) cause the tumour to shrink initially and then to regrow. **(C)** Engineered macrophages and conventional therapy ($P_{bolus} = 250$, $Q_{bolus} = 12$). In 10/10 simulations the tumour is eliminated and normal tissue recovers in 8/10 cases. Key: black solid lines, control (no therapy, mean of ten simulations); black dashed lines, therapy (mean of ten simulations); coloured lines, time course for each of the ten therapy simulations.

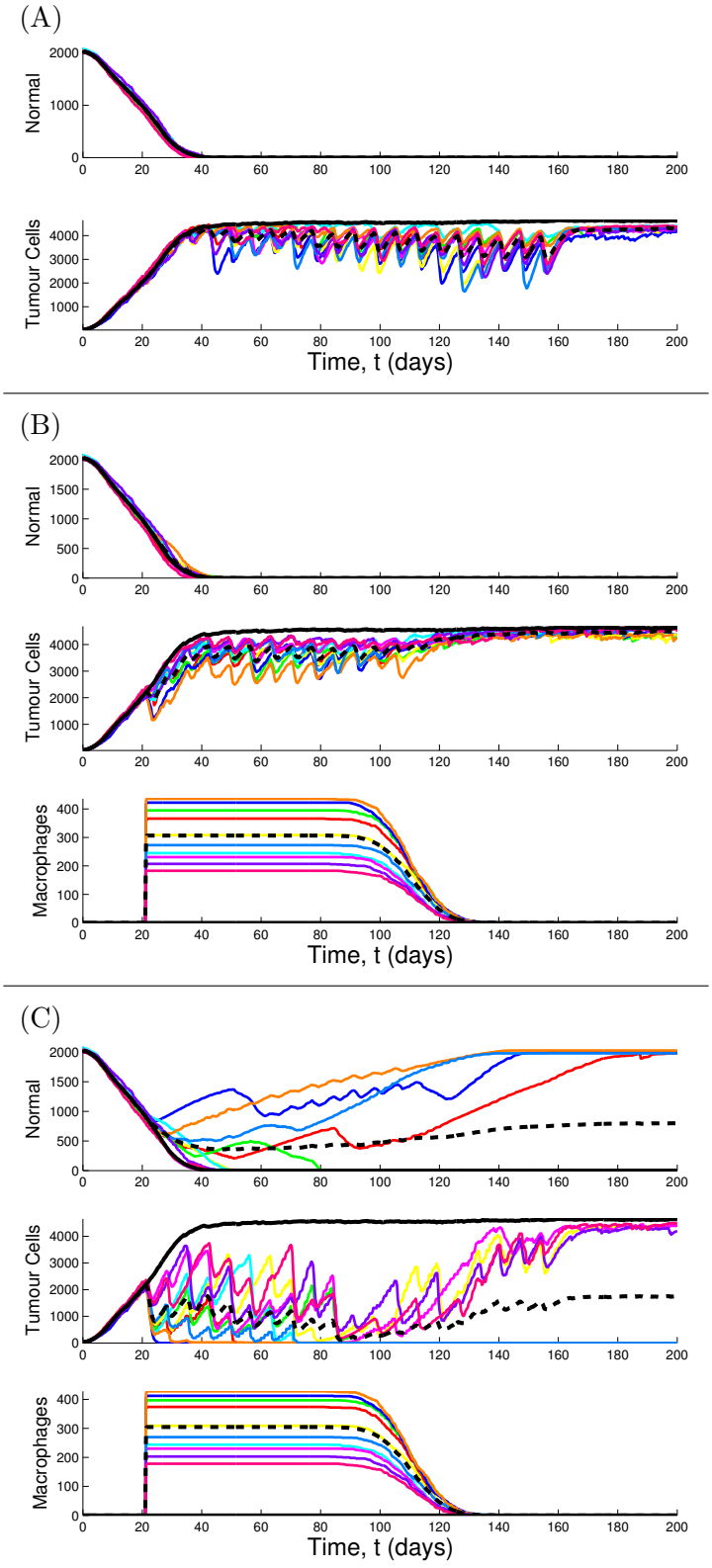

Figure S5: The response to therapy over time. **(A)** Conventional therapy, $Q_{bolus} = 11$. Each bolus leads initially to tumour regression and then regrowth. **(B)** Engineered macrophages accumulate after injection on day 21. Weekly prodrug boluses ($P_{bolus} = 120$) cause the tumour to shrink initially and then to regrow. **(C)** Engineered macrophages and conventional therapy ($P_{bolus} = 120$, $Q_{bolus} = 11$). In 6/10 simulations the tumour is eliminated and normal tissue recovers in 4 of those. Key: black solid lines, control (no therapy, mean of ten simulations); black dashed lines, therapy (mean of ten simulations); coloured lines, time course for each of the ten therapy simulations.

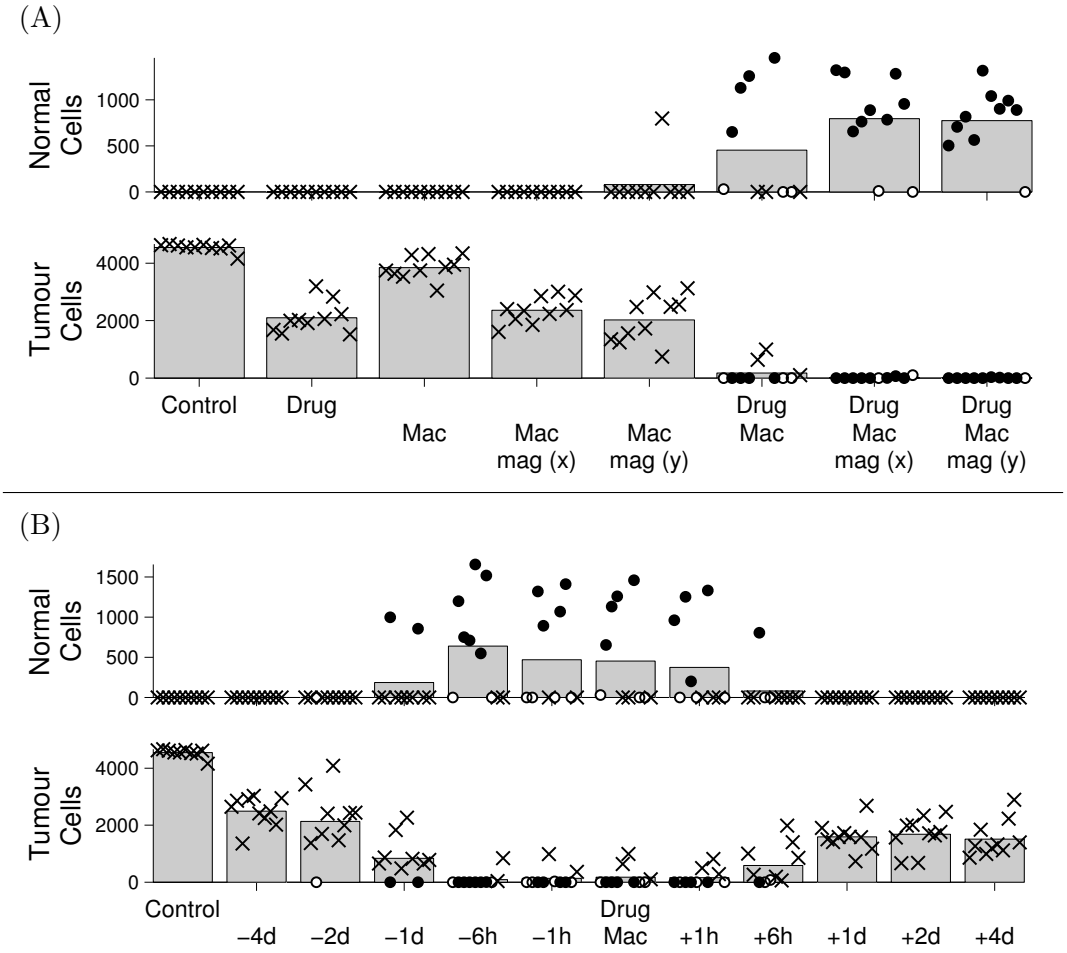

Figure S6: Summary data, showing the state at 100 days for various therapies (with $Q_{bolus} = 12$ and $P_{bolus} = 100$) starting three weeks after tumour implantation. These results demonstrate that the results in the main text are robust to variations in drug and prodrug dose (compare this figure with Figure 7 of the main text). **(A)** The results illustrate the synergistic effects of combination therapies. For example, for combination therapy (drug+macrophages), the average reduction in tumour size is greater than would be expected from the sum of the individual effects. The results also illustrate the variability in response that can occur - for drug+macrophages, in 7/10 simulations the tumour is eliminated, and in 4/10 simulations normal tissue recovers. **(B)** Combination therapy, with various timing shifts of macrophage therapy relative to conventional therapy. "−1h" indicates macrophage therapy is 1 hour before conventional therapy, and this case (along with −6h) gives a small advantage (tumour elimination in 8/10 cases instead of 7/10). Macrophage after conventional therapy is always worse. **(A,B)** Bars represent mean values and individual simulations are indicated by points. The final state of the simulations (at 200 days) is indicated as follows: open circles, tumour and normal cells are eliminated; filled circles, tumour is eliminated and normal cells recover; crosses, tumour persists.

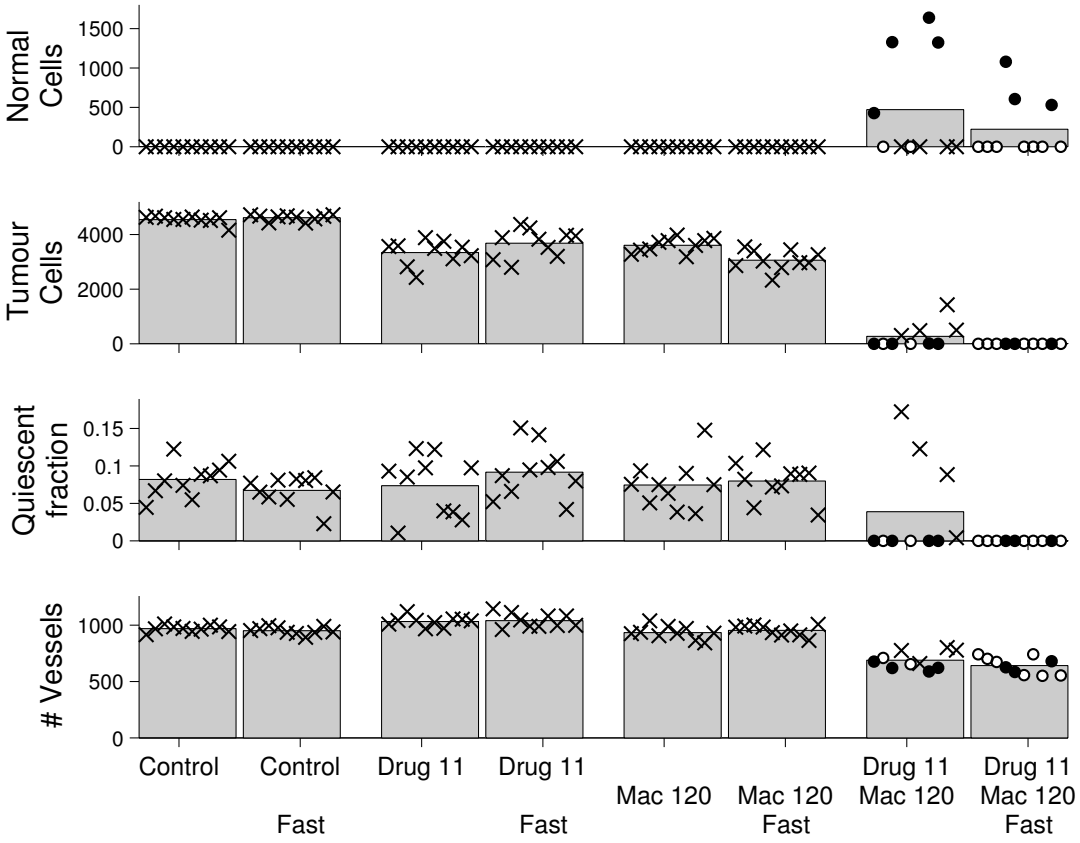

Figure S7: Conventional ($Q_{bolus} = 11$), macrophage ($Q_{bolus} = 120$) and combined therapies with the standard and a doubled maximum cancer cell proliferation rate. With faster cancer proliferation conventional therapy is slightly less effective, whereas macrophage therapy is slightly more effective. Combination therapy is markedly more effective in this case. 'fast' indicates cases with faster cancer cell cycle. These other parameters are the same as in Figure 7 of the main text.

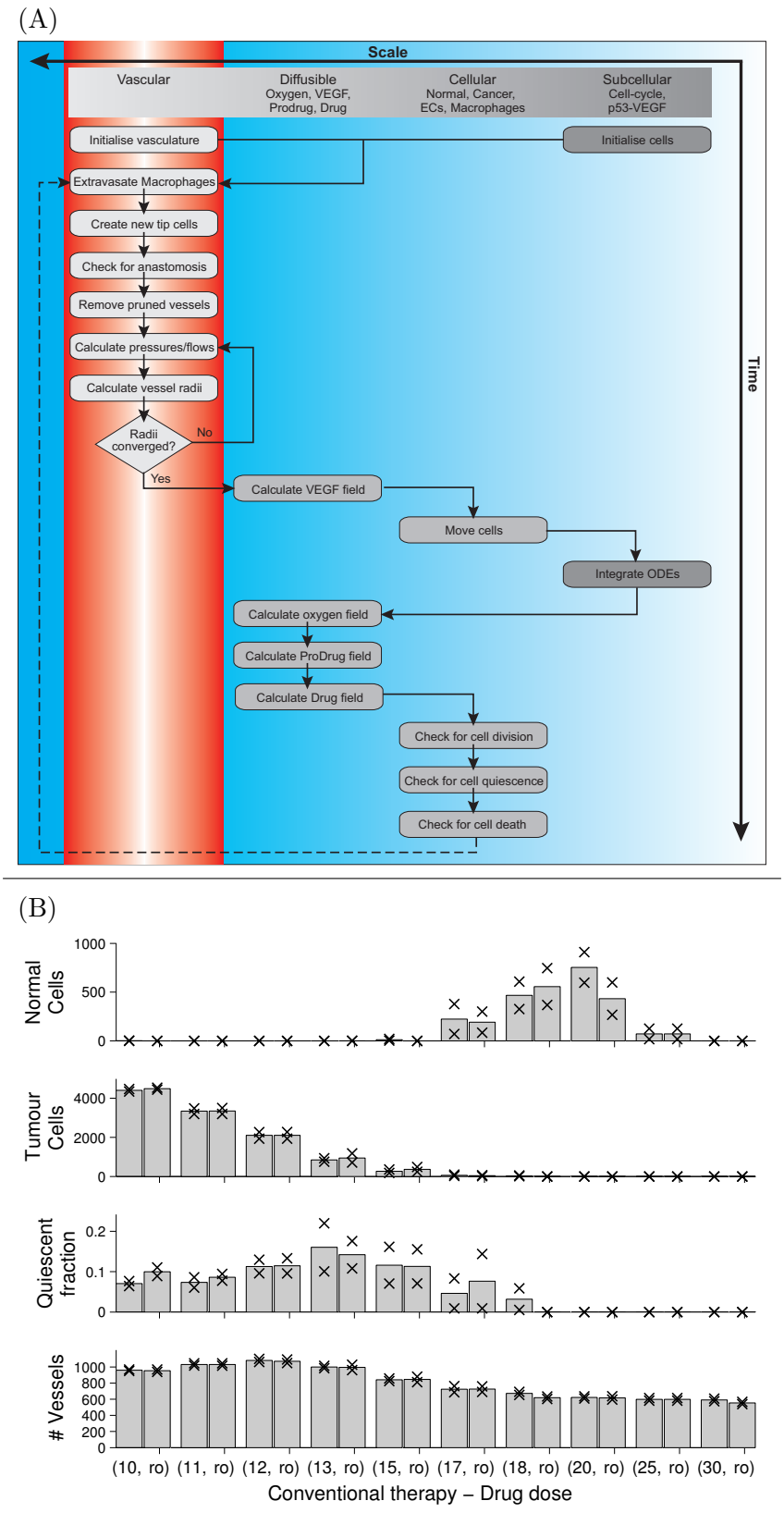

Figure S8: **(A)** Flowchart illustrating an altered ordering of computation (compare with Figure S2). **(B)** Drug dose-response (compare with Figure 5A of the main text) with the standard and alternative ordering of computation, showing that the order does not make much difference. Each pair, '(NN, ro)', on the horizontal axis indicates a drug dose $Q_{bolus} = NN$ with the standard ordering, with 'ro' for the altered ordering. Crosses indicate the mean ± standard error, calculated from 10 simulations for each drug dose.

E Supplementary Movie legends

E.1 Supplementary Movie 1

Typical simulation of macrophage therapy via a single bolus of engineered macrophages three weeks after tumour implantation, coincident with the first of 20 weekly boluses of the prodrug cyclophosphamide. The movie shows the active drug concentration in greyscale, with the different cell types and vascular network superimposed. It is clear that macrophages (yellow) move to hypoxic areas (where quiescent cancer cells are orange), and activate the drug there. To the right we include plots over time of the number of macrophages in the tissue, and the average prodrug and drug concentrations.

E.2 Supplementary Movie 2

Supplementary Movie 2 shows an example simulation involving combination therapy, where three weeks after tumour implantation a single bolus of macrophages is applied, together with the first of 20 weekly doses of prodrug and active drug. The combined treatment eliminates the tumour after 73.5 days, after which the normal tissue recolonises the simulation domain. This synergistic response arises because the combined treatment targets both hypoxic and proliferating tumour cells.

References

[1] A. Akeson, A. Herman, D. Wiginton, and J. Greenberg. Endothelial cell activation in a vegf-a gradient: relevance to cell fate decisions. *Microvasc Res*, 80(1):65–74, Jul 2010.

[2] T. Alarćon, H. M. Byrne, and P. K. Maini. A mathematical model of the effects of hypoxia on the cell-cycle of normal and cancer cells. *J Theor Biol*, 229(3):395–411, 2004.

[3] T. Alarcón, H. M. Byrne, and P. K. Maini. A multiple scale model for tumor growth. *Multiscale Modeling & Simulation*, 3(2):440–475, 2005.

[4] A. R. A. Anderson and M. A. J. Chaplain. Continuous and discrete mathematical models of tumor-induced angiogenesis. *Bull. Math. Biol.*, 60(5):857–899, Sep 1998.

[5] L. W. Anderson, T. L. Chen, O. M. Colvin, L. B. Grochow, J. M. Collins, M. J. Kennedy, and J. M. Strong. Cyclophosphamide and 4-hydroxycyclophosphamide/aldophosphamide kinetics in patients receiving high-dose cyclophosphamide chemotherapy. *Clinical Cancer Research*, 2(9):1481–1487, 09 1996.

[6] R. Audran, B. Collet, A. Moisan, and L. Toujas. Fate of mouse macrophages radiolabelled with pkh-95 and injected intravenously. *Nuclear Medicine and Biology*, 22(6):817–821, 8 1995.

[7] B. Barleon, S. Sozzani, D. Zhou, H. Weich, A. Mantovani, and D. Marme. Migration of human monocytes in response to vascular endothelial growth factor (vegf) is mediated via the vegf receptor flt-1. *Blood*, 87(8):3336–3343, 4 1996.

[8] T. B. Bentley, H. Meng, and R. N. Pittman. Temperature dependence of oxygen diffusion and consumption in mammalian striated muscle. *Am J Physiol*, 264(6 Pt 2):H1825–30, Jun 1993.

[9] A. M. Berezhkovskii and S. M. Bezrukov. Effective drift and diffusion of a particle jumping between mobile and immobile states. *Journal of Electroanalytical Chemistry*, In Press, Corrected Proof.

[10] D. A. Berk, F. Yuan, M. Leunig, and R. K. Jain. Fluorescence photobleaching with spatial fourier analysis: measurement of diffusion in light-scattering media. *Biophysical journal*, 65(6):2428–2436, 12 1993.

[11] D. Bray. *Cell movements: from molecules to motility.* Garland Pub., 2001.

[12] A. S. Brown, L. Leamen, V. Cucevic, and F. S. Foster. Quantitation of hemodynamic function during developmental vascular regression in the mouse eye. *Investigative Ophthalmology & Visual Science*, 46(7):2231–2237, 07 2005.

[13] J. J. Casciari, S. V. Sotirchos, and R. M. Sutherland. Glucose diffusivity in multicellular tumour spheroids. *Cancer Res.*, 48:3905–3909, 1988.

[14] J. J. Casciari, S. V. Sotirchos, and R. M. Sutherland. Variations in tumor cell growth rates and metabolism with oxygen concentration, glucose concentration, and extracellular ph. *Journal of Cellular Physiology*, 151(2):386–394, 1992.

[15] T. K. H. Chang, G. F. Weber, C. L. Crespi, and D. J. Waxman. Differential activation of cyclophosphamide and ifosphamide by cytochromes p-450 2b and 3a in human liver microsomes. *Cancer Research*, 53(23):5629–5637, 12 1993.

[16] T.-C. Chou, H. Dong, X. Zhang, W. P. Tong, and S. J. Danishefsky. Therapeutic cure against human tumor xenografts in nude mice by a microtubule stabilization agent, fludelone, via parenteral or oral route. *Cancer Research*, 65(20):9445–9454, 10 2005.

[17] E. R. Clark. Studies on the growth of blood-vessels in the tail of the frog larva - by observation and experiment on the living animal. *AMERICAN JOURNAL OF ANATOMY*, 23(1):37–88, Jan 1918.

[18] C. Cursiefen, L. Chen, L. P. Borges, D. Jackson, J. Cao, C. Radziejewski, P. A. D'Amore, M. R. Dana, S. J. Wiegand, and J. W. Streilein. VEGF-A stimulates lymphangiogenesis and hemangiogenesis in inflammatory neovascularization via macrophage recruitment. *J Clin Invest*, 113(7):1040–1050, Apr 2004.

[19] J. W. Demmel, S. C. Eisenstat, J. R. Gilbert, X. S. Li, and J. W. H. Liu. A supernodal approach to sparse partial pivoting. *SIAM J. Matrix Analysis and Applications*, 20(3):720–755, 1999.

[20] S. P. Dineen, K. D. Lynn, S. E. Holloway, A. F. Miller, J. P. Sullivan, D. S. Shames, A. W. Beck, C. C. Barnett, J. B. Fleming, and R. A. Brekken. Vascular endothelial growth factor receptor 2 mediates macrophage infiltration into orthotopic pancreatic tumors in mice. *Cancer Research*, 68(11):4340–4346, 06 2008.

[21] DrugBank. Drug card for cyclophosphamide. http://www.drugbank.ca/drugs/DB00531, Jan 2011.

[22] DrugBank. Drug card for doxorubicin. http://www.drugbank.ca/drugs/DB00997, Jan 2011.

[23] R. E. Durand and E. Sham. The lifetime of hypoxic human tumor cells. *International Journal of Radiation Oncology*Biology*Physics*, 42(4):711–715, 11 1998.

[24] A. W. El-Kareh and T. W. Secomb. A mathematical model for comparison of bolus injection, continuous infusion, and liposomal delivery of doxorubicin to tumor cells. *Neoplasia*, 2(4):325–338, Jul-Aug 2000.

[25] A. B. El-Remessy, M. Al-Shabrawey, D. H. Platt, M. Bartoli, M. A. Behzadian, N. Ghaly, N. Tsai, K. Motamed, and R. B. Caldwell. Peroxynitrite mediates vegfs angiogenic signal and function via a nitration-independent mechanism in endothelial cells. *The FASEB Journal*, 21(10):2528–2539, 08 2007.

[26] W. Erl, C. Weber, C. Wardemann, and P. C. Weber. Adhesion properties of mono mac 6, a monocytic cell line with characteristics of mature human monocytes. *Atherosclerosis*, 113(1):99–107, 2 1995.

[27] Y. C. Fung. *Biomechanics: motion, flow, stress, and growth.* Springer-Verlag, New York, 1990.

[28] D. Goldman and A. S. Popel. A computational study of the effect of capillary network anastomoses and tortuosity on oxygen transport. *Journal of Theoretical Biology*, 206(2):181–194, 2000.

[29] R. W. Gore. Quantitative measurements of forces generated by single macrophage and neutrophils migrating in vivo and in vitro. *Biorheology*, 32(2-3), 1995.

[30] A. D. Grief and G. Richardson. Mathematical modelling of magnetically targeted drug delivery. *Journal of Magnetism and Magnetic Materials*, 293(1):455–463, 5 2005.

[31] L. Griffiths, K. Binley, S. Iqball, O. Kan, P. Maxwell, P. Ratcliffe, C. Lewis, A. Harris, S. Kingsman, and S. Naylor. The macrophage - a novel system to deliver gene therapy to pathological hypoxia. *Gene Therapy*, 7:255–262, 2000.

[32] J. Grunstein, W. G. Roberts, O. Mathieu-Costello, D. Hanahan, and R. S. Johnson. Tumor-derived expression of vascular endothelial growth factor is a critical factor in tumor expansion and vascular function. *Cancer Research*, 59(7):1592–1598, 04 1999.

[33] M. Hellstrom, L.-K. Phng, J. J. Hofmann, E. Wallgard, L. Coultas, P. Lindblom, J. Alva, A.-K. Nilsson, L. Karlsson, N. Gaiano, K. Yoon, J. Rossant, M. L. Iruela-Arispe, M. Kalen, H. Gerhardt, and C. Betsholtz. Dll4 signalling through notch1 regulates formation of tip cells during angiogenesis. *Nature*, 445(7129):776–780, 2007.

[34] T. Jackson and X. Zheng. A cell-based model of endothelial cell migration, proliferation and maturation during corneal angiogenesis. *Bulletin of Mathematical Biology*, 72(4):830–868, 2010-05-01.

[35] R. K. Jain. Transport of molecules across tumor vasculature. *Cancer and Metastasis Reviews*, 6(4):559–593, 1987-12-01.

[36] B. H. Jiang, G. L. Semenza, C. Bauer, and H. H. Marti. Hypoxia-inducible factor 1 levels vary exponentially over a physiologically relevant range of o2 tension. *AJP - Cell Physiology*, 271(4):C1172–1180, 10 1996.

[37] H. Kimura, R. D. Braun, E. T. Ong, R. Hsu, T. W. Secomb, D. Papahadjopoulos, K. Hong, and M. W. Dewhirst. Fluctuations in red cell flux in tumor microvessels can lead to transient hypoxia and reoxygenation in tumor parenchyma. *Cancer Res*, 56(23):5522–5528, Dec 1996.

[38] A. G. Koutsiaris, S. V. Tachmitzi, N. Batis, M. G. Kotoula, C. H. Karabatsas, E. Tsironi, and D. Z. Chatzoulis. Volume flow and wall shear stress quantification in the human conjunctival capillaries and post-capillary venules in vivo. *Biorheology*, 44(5-6):375–386, 2007.

[39] S. Kouvroukoglou, K. C. Dee, R. Bizios, L. V. McIntire, and K. Zygourakis. Endothelial cell migration on surfaces modified with immobilized adhesive peptides. *Biomaterials*, 21(17):1725–1733, 9 2000.

[40] F. Y. Lee, D. J. Flannery, and D. W. Siemann. Prediction of tumour sensitivity to 4-hydroperoxycyclophosphamide by a glutathione-targeted assay. *Br J Cancer*, 63(2):217–222, Feb 1991.

[41] F. Mac Gabhann, J. W. Ji, and A. S. Popel. Computational model of vascular endothelial growth factor spatial distribution in muscle and pro-angiogenic cell therapy. *PLoS Computational Biology*, 2(9), 2006.

[42] S. R. McDougall, A. R. A. Anderson, and M. A. J. Chaplain. Mathematical modelling of dynamic adaptive tumour-induced angiogenesis: Clinical implications and therapeutic targeting strategies. *J Theor Biol*, 241(3):564–89, 2006.

[43] A. Meeson, M. Palmer, M. Calfon, and R. Lang. A relationship between apoptosis and flow during programmed capillary regression is revealed by vital analysis. *Development*, 122(12):3929–3938, 1996.

[44] M. Muthana, S. D. Scott, N. Farrow, F. Morrow, C. Murdoch, S. Grubb, N. Brown, J. Dobson, and C. E. Lewis. A novel magnetic approach to enhance the efficacy of cell-based gene therapies. *GENE THERAPY*, 15(12):902–910, Jun 2008.

[45] M. R. Owen, T. Alarcón, P. K. Maini, and H. M. Byrne. Angiogenesis and vascular remodelling in normal and cancerous tissues. *J Math Biol*, 58(4-5):689–721, Apr 2009.

[46] M. R. Owen and J. A. Sherratt. Pattern formation and spatiotemporal irregularity in a model for macrophage-tumour interactions. *J. Theor. Biol.*, 189:63–80, 1997.

[47] K. J. Painter and T. Hillen. Volume-filling and quorum-sensing in models for chemosensitive movement. *Can. Appl. Math. Q.*, 10(4):501–543, 2002.

[48] A. R. Pries, B. Reglin, and T. W. Secomb. Structural adaptation of microvascular networks: functional roles of adaptive responses. *Am J Physiol Heart Circ Physiol*, 281(3):H1015–25, 2001.

[49] A. R. Pries, T. W. Secomb, and P. Gaehtgens. Design principles of vascular beds. *Circulation Research*, 77(5):1017–1023, 1995.

[50] A. R. Pries, T. W. Secomb, and P. Gaehtgens. Structural adaptation and stability of microvascular networks: theory and simulations. *AJP - Heart and Circulatory Physiology*, 275(2):H349–360, 1998.

[51] N. Resnick, H. Yahav, A. Shay-Salit, M. Shushy, S. Schubert, L. C. M. Zilberman, and E. Wofovitz. Fluid shear stress and the vascular endothelium: for better and for worse. *Progress in Biophysics and Molecular Biology*, 81(3):177–199, 2003.

[52] B. Ribba, K. Marron, Z. Agur, T. Alarcon, and P. K. Maini. A mathematical model of doxorubicin treatment efficacy for non-hodgkin's lymphoma: investigation of the current protocol through theoretical modelling results. *Bull Math Biol*, 67(1):79–99, Jan 2005.

[53] J. A. Ross and M. J. Auger. The biology of the macrophage. In B. Burke and C. E. Lewis, editors, *The Macrophage*. Oxford University Press, 2nd edition, 2002.

[54] J. Royds, S. Dower, E. Qwarnstrom, and C. Lewis. Response of tumour cells to hypoxia: role of p53 and nfkb. *British Medical Journal*, 51(2):55, 1998.

[55] T. W. Secomb, R. Hsu, and M. W. Dewhirst. Synergistic effects of hyperoxic gas breathing and reduced oxygen consumption on tumor oxygenation: a theoretical model. *International Journal of Radiation Oncology Biology Physics*, 59(2):572–578, 6 2004.

[56] R. Serban, C. Woodward, and A. Hindmarsh. Sundials (SUite of Nonlinear and DIfferential/ALgebraic equation Solvers). https://computation.llnl.gov/casc/sundials/main.html, Jan 2011.

[57] J. A. Sherratt and J. D. Murray. Models of epidermal wound healing. *Proc. R. Soc. Lond. B*, 241:29–36, 1990.

[58] M. Shimpo, U. Ikeda, Y. Maeda, M. Takahashi, H. Miyashita, H. Mizukami, M. Urabe, A. Kume, T. Takizawa, M. Shibuya, K. Ozawa, and K. Shimada. Aav-mediated vegf gene transfer into skeletal muscle stimulates angiogenesis and improves blood flow in a rat hindlimb ischemia model. *Cardiovascular Research*, 53(4):993–1001, 03 2002.

[59] A. Srivastava, P. Laidler, R. P. Davies, K. Horgan, and L. E. Hughes. The prognostic significance of tumor vascularity in intermediate-thickness (0.76-4.0 mm thick) skin melanoma. a quantitative histologic study. *Am J Pathol*, 133(2):419–423, Nov 1988.

[60] M. Stefanini, F. Wu, F. Mac Gabhann, and A. Popel. A compartment model of vegf distribution in blood, healthy and diseased tissues. *BMC Systems Biology*, 2(1):77, 2008.

[61] C. Stokes, D. Lauffenburger, and S. Williams. Migration of individual microvessel endothelial cells: stochastic model and parameter measurement. *Journal of Cell Science*, 99(2):419–430, 1991.

[62] C. L. Stokes and D. A. Lauffenburger. Analysis of the roles of microvessel endothelial cell random motility and chemotaxis in angiogenesis. *Journal of Theoretical Biology*, 152(3):377–403, 1991.

[63] B. R. Stoll, C. Migliorini, A. Kadambi, L. L. Munn, and R. K. Jain. A mathematical model of the contribution of endothelial progenitor cells to angiogenesis in tumors: implications for antiangiogenic therapy. *Blood*, 102(7):2555–2561, 2003.

[64] S. Suchting, C. Freitas, F. le Noble, R. Benedito, C. Breant, A. Duarte, and A. Eichmann. The notch ligand delta-like 4 negatively regulates endothelial tip cell formation and vessel branching. *Proceedings of the National Academy of Sciences*, 104(9):3225–3230, 2007.

[65] J. J. Tyson and B. Novak. Regulation of the eukaryotic cell cycle: Molecular antagonism, hysteresis, and irreversible transitions. *J. Theor. Biol.*, 210:249–263, 2001.

[66] E. N. Unemori, N. Ferrara, E. A. Bauer, and E. P. Amento. Vascular endothelial growth factor induces interstitial collagenase expression in human endothelial cells. *Journal of Cellular Physiology*, 153(3):557–562, 1992.

[67] R. Wagner. Mersenne twister random number generator. http://www-personal.umich.edu/ wagnerr/MersenneTwister.html, Jan 2011.

[68] N. Weidner, J. P. Semple, W. R. Welch, and J. Folkman. Tumor angiogenesis and metastasis–correlation in invasive breast carcinoma. *N Engl J Med*, 324(1):1–8, Jan 1991.

[69] N. Z. Wu, B. Klitzman, G. Rosner, D. Needham, and M. W. Dewhirst. Measurement of material extravasation in microvascular networks using fluorescence video-microscopy. *Microvascular Research*, 46(2):231–253, 9 1993.

[70] C. V. Zerbinatti and R. W. Gore. Uptake of modified low-density lipoproteins alters actin distribution and locomotor forces in macrophages. *Am J Physiol Cell Physiol*, 284(2):555–561, Feb 2003.